City Research Online

# City, University of London Institutional Repository

This is the published version of the paper.

This version of the publication may differ from the final published version.

Original Article

# Integrated effects of auxeticity and pyro-coupling on the nonlinear static behaviour of magneto-electro-elastic sandwich plates subjected to multi-field interactive loads

Vinyas Mahesh (ORCID)

## Abstract

This work presents a detailed investigation of the effect of auxeticity synergised with the pyro-coupling behaviour of multiphase magneto-electro-elastic (M-MEE) composites using a finite element (FE) framework. The nonlinear deflection and bending problems of sandwich plates with auxetic core and M-MEE skins subjected to multi-physics load (electric, magnetic and thermal) are probed. The plate kinematics is governed by Reddy's higher-order shear deformation theory (HSDT). The nonlinear relation between the strains and displacements is established through von-Karman's nonlinear relations. The temperature profiles are considered linearly and nonlinearly varying across the thickness of the plate. Various parametric studies presented in this article highlight the influence of the auxetic cell inclination angle, rib-length ratio, rib thickness, the plate-to-core ratio etc., associated with the pyro-coupling on the nonlinear deflection and bending of sandwich plates. The results reveal that the plate deflection, bending behaviour and degree of pyro-coupling significantly depend on the auxetic unit cell dimensions and magnitude of electro-magnetic loads. The significant influence of temperature profiles on the pyro-coupling are witnessed at lower auxetic cell angle. The nonlinear deflections of the sandwich plate and hence the potentials developed tend to improve with the lower values of plate-to-core ratio and rib thickness. The prominent outcomes of this work related to integrated effects of auxeticity and pyro-coupling are not yet reported in the open literature and are deemed to be utilised as a future reference.

## Introduction

Auxetic materials represent the class of current frontiers in material development due to their structural properties characterised by a negative Poisson's ratio.[1] They characterise an opposite trend of deformation than the conventional and incompressible materials. They are also termed anti-rubber materials. Auxetics exhibit enhanced toughness, shear resistance, resilience, damping, acoustics and high load bearing capacity. Further, auxetics significantly influences the deformation of the structure and, thereby, its stress distributions. Considering these benefits of auxetics, several researchers have rigorously worked on analysing its structural response. Hou et al.[2] experimentally assessed the effect of using auxetic cores on the bending and failure of the sandwich structure. The experimental data was reinforced with

the numerical analysis as well. The effectiveness of using auxetic cores in enhancing the blast resistance of structures was numerically justified by Jin et al.[3] Li et al.[4] predicted the nonlinear bending characteristics of sandwich beams with functionally graded (FG) auxetic cores operated in a thermal environment. Boldrin et al.[5] studied the vibroacoustic behaviour of auxetic composite structures using full-scale finite elements (FE). The influence of the thermal environment associated with the auxeticity of sandwich beams was probed by Li et al.[6] The same research group[7] also

Department of Engineering, City, University of London, London, UK

**Corresponding author:**
Vinyas Mahesh, Department of Engineering, City, University of London, London EC1V 0HB, UK.
Emails: vinyas.mahesh@gmail.com; vinyas.mahesh@city.ac.uk

presented the nonlinear dynamic characteristics of sandwich beams with FG auxetic core. The auxetics combined with other variants of conventional sandwich structures[8–15] can tremendously benefit the engineering domain by increased weight reduction and structural integrity.

Smart materials provide additional flexibility and tailorability to engineers in designing structures with enhanced integrity. Piezoelectric, piezomagnetic, thermo-electric and other materials are exploited for this purpose. However, with the recent advancement in material science, a new class of smart materials known as magneto-electro-elastic (MEE) composites has grasped the researchers' attention.[16] The multifield interaction between the various fields exhibited by MEE composites makes them a potential candidate for various engineering applications, including vibration control,[17–23] energy harvesting[24–27] and impact engineering.[28–30] Zhao et al.[31] predicted the nonlinear response of multiphase MEE plates reinforced with CNTs. Zhou et al.[32] proposed an element-free Galerkin method to investigate the MEE structural problems. Quang et al.[33] presented an analytical model to assess the static buckling of MEE sandwich structure subjected to Multi-physics loads. Dinh Dat et al.[34] probed the effect of blast loads on the dynamic behaviour of MEE plates with auxetic cores. Nie et al.[35] developed a stable node-based smoothed radial point interpolation method to examine the dynamic response of MEE structures.

Due to the multifield interactive capability of the MEE composites, it exhibits thermo-electric and thermo-magnetic coupling when operated in the thermal environment. These are termed 'pyro-coupling' effects. Several kinds of research have been reported on the thermal analysis of smart MEE structures, but a few focus on the pyro-coupling effects on the structural responses. Vinyas and Kattimani[36,37] showed that pyro-coupling enhances the multifunctionality of the stepped functionally graded MEE beams and plates. In addition, Vinyas et al. and his group conducted several pilot studies on various structural responses of MEE composites operated in the thermal environment highlighting the influence of pyro-coupling.[38–42]

The deflections of the structure in the nonlinear regime seriously threaten its optimal performance. Hirwani and Panda[43] assessed the nonlinear deformations of pre-damaged composite panels subjected to thermo-mechanical loads using the FE approach. Chen and Chen[44] probed the influence of initial tension on the large deflections of the isotropic layered plate through an analytical approach. Exploiting the kp-Ritz method, the nonlinear deflections of carbon nanotube (CNT) reinforced panels were investigated by Zhang et al.[45] The influence of elastic foundation on the nonlinear deflections of theta ply laminates was studied by Alamatian and Golmakani[46] using kinetic dynamic relaxation. Sepahi et al.[47] assessed the nonlinear deflections of functionally graded (FG) annular plates under thermo-mechanical load using the differential quadrature method. Tiar et al.[48] proposed a FE formulation to examine the large deflections of 2D composite structures. The variation of the large thermomechanical deflections of FG CNT shell subjected to various forms of mechanical loads was studied by Mehar and Panda.[49] Gholami and Ansari[50] investigated the influence of graphene reinforcement on the large deflections of composite plates. Mareishi et al.[51] studied the effect of piezoelectric skins on composite beams' large deflections through an analytical approach. On the same grounds, focussing on the nonlinear structural response of MEE composites, Sh et al.[52] investigated the influence of porosity on the nonlinear transient response functionally graded MEE plates. Similarly, Mahesh and Harursampath[53] studied the nonlinear deflections of porous MEE plate. Quan et al.[54] analytically studied the nonlinear dynamic response of imperfect MEE plate with volume fraction equal of 1. Mahesh et al.[55] studied the influence of auxeticity on the natural frequency of MEE cell structures. The effects of CNT reinforcement and micro-topological textures on the nonlinear responses of MEE plates have been reported in Mahesh and Harursampath.[56,57]

From the literature review, it was realised, to the best of the author's knowledge, that no work has been reported on investigating the inter-dependency of auxeticity and multi-physics loads with the pyro-coupling characteristics of sandwich MEE composites. This motivated the authors to examine sandwich plates' nonlinear deflection and bending response with auxetic core and M-MEE skins, subject to linear and nonlinear temperature profiles and electro-magnetic loads, for the first time. In addition, the influence of different auxetic cell dimensions such as inclination angle, rib-length ratio, rib-thickness etc., are considered for the evaluation. Furthermore, this work is carried out using the FE approach owing to its simplicity in incorporating multi-field interactions and efficiency in capturing the complex structural responses accurately.[58–61] It is believed that the outcomes of this work will lead to novel designs of light-weight smart structures for integrated structural health monitoring and management applications.

## Problem description

The sandwich plate is composed of the auxetic core with multiphase MEE (M-MEE) skins as shown in Figure 1(a) and subjected to a temperature environment which can be explicitly represented as[62]:

$$T(z) = (T_{ts} - T_{bs})\left\{\frac{z}{h} + \frac{1}{2}\right\}^{\upsilon} + T_{bs} \qquad (1)$$

where, $T_{ts}$ and $T_{bs}$ represent the temperature on the top and bottom surfaces of the sandwich plate. Meanwhile, $\upsilon$ denotes the temperature gradient
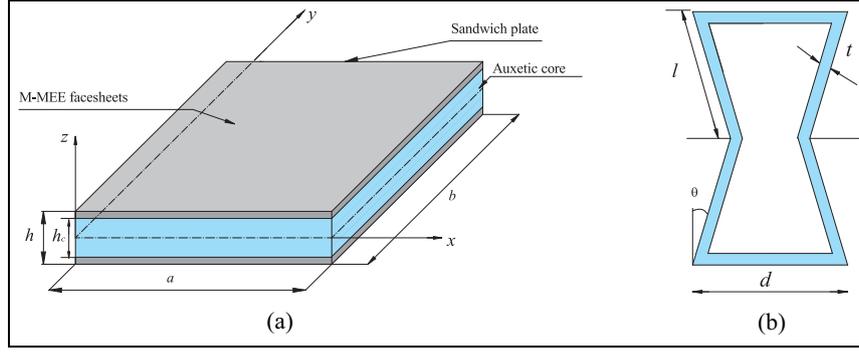
**Figure 1.** Schematic of the: (a) sandwich plate geometry and (b) auxetic unit cell.

exponent, which can take up values between 1 and $\infty$. For linear temperature profiles (LTP), $\nu = 1$, whereas the rest of the higher positive values result in nonlinear temperature profiles (NTP).

The core of the sandwich plate is made of auxetic unit cells whose geometrical dimensions are depicted in Figure 1(b). The length of horizontal and inclined ribs is represented by $l$ and $d$. The auxetic cell inclination angle is shown by $\theta$. The rib thickness is denoted by $t$. The M-MEE skin comprises 50% BaTiO$_3$ and 50% CoFe$_2$O$_4$, whose material properties are shown in Table 1.

## Materials and methods

The material properties related to the auxetic core of the sandwich plate can be expressed as[6]:

$$E_1^{(c)} = E^c \frac{(t/l)^3((d/l) - \sin\theta)}{\cos\theta\left[1 + (\tan^2\theta + (d/l)\sec^2\theta)(t/l)^2\right]},$$

$$E_2^{(c)} = E^c \frac{(t/l)^3}{\cos\theta((d/l) - \sin\theta)\left(\tan^2\theta + (t/l)^2\right)},$$

$$G_{12}^{(c)} = G^c \frac{(t/l)^3}{(d/l)(1 + 2(d/l))\cos\theta}, \; G_{23}^{(c)} = G^c \frac{(t/l)\cos\theta}{(d/l) - \sin\theta},$$

$$G_{13}^{(c)} = G^c \frac{(t/l)}{2\cos\theta}\left[\frac{(d/l) - \sin\theta}{1 + 2(d/l)} + \frac{(d/l) + 2\sin^2\theta}{2((d/l) - \sin\theta)}\right],$$

$$v_{12}^{(c)} = -\frac{\sin\theta\left(1 - (t/l)^2\right)((d/l) - \sin\theta)}{\cos^2\theta\left[1 + (\tan^2\theta + \sec^2\theta(d/l))(t/l)^2\right]},$$

$$v_{21}^{(c)} = -\frac{\sin\theta\left(1 - (t/l)^2\right)}{\left(\tan^2\theta + (t/l)^2\right)((d/l) - \sin\theta)},$$

$$\rho^c = \rho\frac{(t/l)((d/l) + 2)}{2\cos\theta((d/l) - \sin\theta)}\alpha_1^{(c)} = \alpha_m\frac{(t/l)\cos\theta}{(\sin\theta + \alpha)};$$

$$\alpha_2^{(c)} = \alpha_m\frac{(t/l)((d/l) + \sin\theta)}{((2d/l) + 1)\cos\theta}$$

$$(2)$$

The elastic modulus, shear modulus and density of the auxetic core are represented by $E^c$, $G^c$ and rc, respectively. Also, the core's Poisson ratio is denoted as $v^c_{21}$ and $v^c_{12}$.

**Table 1.** Coupled properties of multiphase MEE (50% BaTiO$_3$-50% CoFe$_2$O$_4$ composite).

| Material property | Material constants | 0.5 $V_f$ (50% PE + 50% PM) |
|---|---|---|
| Elastic constants (GPa) | $C_{11} = C_{22}$ | 220 |
| | $C_{12}$ | 120 |
| | $C_{13} = C_{23}$ | 120 |
| | $C_{33}$ | 215 |
| | $C_{44} = C_{55}$ | 45 |
| | $C_{66}$ | 50 |
| Piezoelectric constants (C/m$^2$) | $e_{31} = e_{32}$ | −3.5 |
| | $e_{33}$ | 9.0 |
| | $e_{15} = e_{24}$ | 0 |
| Dielectric constant (10$^{-9}$ C$^2$/Nm$^2$) | $\eta_{11} = \eta_{22}$ | 0.85 |
| | $\eta_{33}$ | 6.3 |
| Magnetic permeability (10$^{-4}$ Ns$^2$/C$^2$) | $\mu_{11} = \mu_{22}$ | −2.0 |
| | $\mu_{33}$ | 0.9 |
| Piezomagnetic constants (N/Am) | $q_{31} = q_{32}$ | 350 |
| | $q_{33}$ | 320 |
| | $q_{15} = q_{24}$ | 200 |
| Magneto-electric constant (10$^{-12}$ Ns/VC) | $m_{11} = m_{22}$ | 5.5 |
| | $m_{33}$ | 2600 |
| Pyroelectric-constant (10$^{-7}$ C/m$^2$K) | $p_2$ | −7.8 |
| Pyromagnetic constant (10$^{-5}$ C/m$^2$K) | $\tau_2$ | −23 |
| Thermal expansion coefficient (10$^{-6}$ K$^{-1}$) | $\alpha_1 = \alpha_2$ | 12.3 |
| | $\alpha_3$ | 8.2 |
| Density (kg/m$^3$) | $\rho$ | 5550 |

Analogously, the constitutive equations of M-MEE facings are as follows[36]:

$$\{\sigma\} = [Q]\{\varepsilon\} - [e]\{E\} - [q]\{H\} - [Q][\alpha]\Delta T$$

$$\{D\} = [e]^T\{\varepsilon\} + [\eta]\{E\} + [m]\{H\} + [p]\Delta T \quad (3)$$

$$\{B\} = [q]^T\{\varepsilon\} + [m]\{E\} + [\mu]\{H\} + [\tau]\Delta T$$

The matrix $[Q]$ encapsulates the coupled elastic coefficients, $[e]$ and $[q]$ denote the matrix of piezoelectric and magnetostrictive coefficients. Similarly, $[m]$, $[\eta]$ and $[\mu]$ show the matrices of electro-magnetic, dielectric and magnetic permeability coefficients. The pyroelectric and pyro-magnetic coefficients are denoted by $[p]$ and $[\tau]$.

The variation of the potentials across the plate's thickness can be assumed as follows[40,41]:

$$
\phi^{\mathrm{u}} = \left(\frac{z - h_3}{h}\right)\overline{\phi}; \phi^{\mathrm{l}} = \left(\frac{h_2 - z}{h}\right)\overline{\phi}; \phi = \phi^{\mathrm{u}} + \phi^{\mathrm{l}}
$$

$$
\psi^{\mathrm{u}} = \left(\frac{z - h_3}{\mathrm{h}}\right)\overline{\psi}; \psi^{\mathrm{l}} = \left(\frac{h_2 - z}{\mathrm{h}}\right)\overline{\psi}; \psi = \psi^{\mathrm{u}} + \psi^{\mathrm{l}}
$$

(4)

The terms $\varphi^u$ and $\psi^u$ denote the variation of the electric and magnetic potentials on the upper facesheet, whereas $\varphi^l$ and $\psi^l$ represent the same for the lower facesheet. Meanwhile, the summation of the potentials of upper and lower skins are denoted by $\varphi$ and $\psi$, respectively.

$h_3$ and $h_2$ denote the top layer of the upper facesheet and the bottom layer of the lower facesheet, respectively.

## Displacement model

The sandwich plate kinematics is governed by the HSDT, whose displacements in the $x$, $y$ and $z$ axes are as follows[63]:

$$
u = u_0 + z\theta_x - \frac{4}{3h^2}z^3\left(\theta_x + \frac{\partial w_0}{\partial x}\right)
$$

$$
v = v_0 + z\theta_y - \frac{4}{3h^2}z^3\left(\theta_y + \frac{\partial w_0}{\partial y}\right)
$$

$$
w = w_0
$$

(5)

## Nonlinear strain-displacement relation

The following is the nonlinear relation between the strains (bending $\{\varepsilon_b\}$ and shear $\{\varepsilon_s\}$ strains) and displacements[40]:

$$
\{\varepsilon_b\} = \left\{\begin{array}{c} \varepsilon_x \\ \varepsilon_y \\ \gamma_{xy} \end{array}\right\} = \left\{\begin{array}{c} \frac{\partial u_o}{\partial x} + \frac{1}{2}\left(\frac{\partial w_o}{\partial x}\right)^2 \\ \frac{\partial v_o}{\partial y} + \frac{1}{2}\left(\frac{\partial w_o}{\partial y}\right)^2 \\ \frac{\partial u_o}{\partial y} + \frac{\partial v_o}{\partial x} + \frac{\partial w_o}{\partial x} \cdot \frac{\partial w_o}{\partial y} \end{array}\right\}
$$

$$
+ z\left\{\begin{array}{c} \frac{\partial \theta_x}{\partial x} \\ \frac{\partial \theta_y}{\partial y} \\ \frac{\partial \theta_x}{\partial y} + \frac{\partial \theta_y}{\partial x} \end{array}\right\} - \frac{4z^3}{3h^2}\left\{\begin{array}{c} \frac{\partial \theta_x}{\partial x} + \frac{\partial^2 w_o}{\partial x^2} \\ \frac{\partial \theta_y}{\partial y} + \frac{\partial^2 w_o}{\partial y^2} \\ \frac{\partial \theta_x}{\partial y} + \frac{\partial \theta_y}{\partial x} + 2\frac{\partial^2 w_o}{\partial x \partial y} \end{array}\right\}
$$

(6)

$$
\{\varepsilon_s\} = \left\{\begin{array}{c} \gamma_{xz} \\ \gamma_{yz} \end{array}\right\} = \left\{\begin{array}{c} \theta_x + \frac{\partial w_o}{\partial x} \\ \theta_y + \frac{\partial w_o}{\partial y} \end{array}\right\} - \frac{4z^2}{h^2}\left\{\begin{array}{c} \theta_x + \frac{\partial w_o}{\partial x} \\ \theta_y + \frac{\partial w_o}{\partial y} \end{array}\right\}
$$

(7)

## Finite element formulation

The eight-noded isoparametric element with nine degrees of freedom at each node is used to discretise the sandwich plates. They are grouped into displacement and potentials, with designations like $\{s_t\}, \{s_r\}, \{s_{r*}\}, \psi$ and $\phi$. They can also be expressed using shape functions, such as[41]

$$
\{s_r\} = [N_r]\{s_r^e\}; \{s_{r*}\} = [N_{r*}]\{s_{r*}^e\}
$$

$$
\phi = [N_\phi]\{\phi^e\}; \psi = [N_\psi]\{\psi^e\}
$$

(8)

in which,

$$
\{s_t^e\} = \left[\{s_{t1}^e\}^T \quad \{s_{t2}^e\}^T \quad \cdots \{s_{t8}^e\}^T\right]^T, \{s_r^e\}
$$

$$
= \left[\{s_{r1}^e\}^T \quad \{s_{r2}^e\}^T \quad \cdots \{s_{r8}^e\}^T\right]^T,
$$

$$
\{s_{r*}^e\} = \left[\{s_{r*1}^e\}^T \quad \{s_{r*2}^e\}^T \quad \cdots \{s_{r*8}^e\}^T\right]^T
$$

(9)

and

$$
\{s_{ti}\} = \begin{bmatrix} u_{0i} & v_{0i} & w_{0i} \end{bmatrix}^T, \{s_{ri}\} = \begin{bmatrix} \theta_{xi}\theta_{yi} \end{bmatrix}^T,
$$

$$
\{s_{r*i}\} = \begin{bmatrix} \kappa_{xi}\kappa_{yi} \end{bmatrix}^T.
$$

(10)

The components of the bending strain of equation (6) include linear and nonlinear strains as follows[41]:

$$
\{\varepsilon_b\} = \{\varepsilon_{b\_L}\} + \{\varepsilon_{b\_NL}\}
$$

(11)

In terms of FE quantities, the strains can be expressed as

$$
\{\varepsilon_{b\_L}\} = [SD_{tb}]\{s_t\} + z[SD_{rb}]\{s_r\} + c_1 z^3[SD_{rb}]\{s_r\}
$$

$$
+ c_1 z^3[SD_{rb}]\{s_{r*}\}
$$

$$
\{\varepsilon_{b\_NL}\} = \frac{1}{2}[SD_1][SD_2]\{s_t\}
$$

(12)

Therefore, equation (11) can be re-written as follows:

$$
\{\varepsilon_b\} = [SD_{tb}]\{s_t\} + z[SD_{rb}]\{s_r\} + c_1 z^3[SD_{rb}]\{s_r\}
$$

$$
+ c_1 z^3[SD_{rb}]\{s_{r*}\} + \frac{1}{2}[SD_1][SD_2]\{s_t\}
$$

(13)

Similarly, the shear strains can be expressed as

$$
\{\varepsilon_s\} = [SD_{ts}]\{s_t\} + [SD_{rs}]\{s_r\} + c_2 z^2[SD_{rs}]\{s_r\}
$$

$$
+ c_2 z^2[SD_{rs}]\{s_{r*}\}
$$

(14)

The electric and magnetic fields throughout the thickness of the M-MEE facesheets may be represented using Maxwell's equation as follows, depending on the variation of the potentials considered. as follows[41]:

$$\{E\} = \left\{\begin{matrix} E_x^u \\ E_y^u \\ E_z^u \end{matrix}\right\} + \left\{\begin{matrix} E_x^l \\ E_y^l \\ E_z^l \end{matrix}\right\} = \left\{\begin{matrix} \frac{-\partial\phi^u}{\partial x} \\ \frac{-\partial\phi^u}{\partial y} \\ \frac{-\partial\phi^u}{\partial z} \end{matrix}\right\} + \left\{\begin{matrix} \frac{-\partial\phi^l}{\partial x} \\ \frac{-\partial\phi^l}{\partial y} \\ \frac{-\partial\phi^l}{\partial z} \end{matrix}\right\}$$

$$\{H\} = \left\{\begin{matrix} H_x^u \\ H_y^u \\ H_z^u \end{matrix}\right\} + \left\{\begin{matrix} H_x^l \\ H_y^l \\ H_z^l \end{matrix}\right\} = \left\{\begin{matrix} \frac{-\partial\psi^u}{\partial x} \\ \frac{-\partial\psi^u}{\partial y} \\ \frac{-\partial\psi^u}{\partial z} \end{matrix}\right\} + \left\{\begin{matrix} \frac{-\partial\psi^l}{\partial x} \\ \frac{-\partial\psi^l}{\partial y} \\ \frac{-\partial\psi^l}{\partial z} \end{matrix}\right\}$$

$$(15)$$

in terms of FE parameters, it can be written as

$$
\begin{aligned}
E &= -[Z_t][SD_\phi]\{\phi^e\} - [Z_b][SD_\phi]\{\phi^e\} \\
H &= -[Z_t][SD_\psi]\{\psi^e\} - [Z_b][SD_\psi]\{\psi^e\}
\end{aligned}
\tag{16}
$$

where,

$$[Z_t] = \frac{1}{h}\begin{bmatrix} 0 & 0 & 0 \\ 0 & 0 & 0 \\ 0 & 0 & z - h_3 \end{bmatrix}; [Z_b] = \frac{1}{h}\begin{bmatrix} 0 & 0 & 0 \\ 0 & 0 & 0 \\ 0 & 0 & h_2 - z \end{bmatrix}$$

$$(17)$$

### The total potential energy principle

The total potential energy for the sandwich plate with auxetic core and M-MEE skins can be written as follows[36]:

$$\delta T_p = \sum_{N=1}^{3}$$

$$
\begin{aligned}
&\left[ \frac{1}{2}\int_{\Omega^N} \delta\{\varepsilon_b\}^T\{\sigma_b\}d\Omega^N + \frac{1}{2}\int_{\Omega} \delta\{\varepsilon_s\}^T\{\sigma_s\}d\Omega^N - \frac{1}{2}\int_{\Omega^N} \delta\{E\}^T\{D\}d\Omega^N \right. \\
&\left. - \frac{1}{2}\int_{\Omega^N} \delta\{H\}^T\{B\}d\Omega^N \right] - \int_A \phi Q^\phi dA - \int_A \psi Q^\psi dA = 0
\end{aligned}
$$

$$(18)$$

Replacing the terms of equation (18) with the constitutive equations (equation (3)) and FE entities (equations (8)–(14)) and further condensing based on the degrees of freedom as shown in Appendix A, the equations of motion can be written as follows[41]:

$$
\begin{aligned}
&([S_1] + [S_{NL1}])\{s_t\} + ([S_2] + [S_{NL2}])\{s_r\} \\
&\quad + ([S_3] + [K_{NL3}])\{s_{r*}\} + ([S_4] + [S_{NL4}])\{\phi\} \\
&\quad + ([S_5] + [S_{NL5}])\{\psi\} = \{F_T\}
\end{aligned}
$$

$$(19.a)$$

$$
\begin{aligned}
&([S_6] + [S_{NL6}])\{s_t\} + [S_7]\{s_r\} + [S_8]\{s_{r*}\} + [S_9]\{\phi\} \\
&\quad + [S_{10}]\{\psi\} = 0
\end{aligned}
$$

$$(19.b)$$

$$
\begin{aligned}
&([S_{11}] + [S_{NL7}])\{s_t\} + [S_{12}]\{s_r\} + [S_{13}]\{s_{r*}\} \\
&\quad + [S_{14}]\{\phi\} + [S_{15}]\{\psi\} = 0
\end{aligned}
$$

$$(19.c)$$

$$
\begin{aligned}
&([S_{16}] + [S_{NL8}])\{s_t\} + [S_{17}]\{s_r\} + [S_{18}]\{s_{r*}\} \\
&\quad + [S_{\phi\phi}]\{\phi\} + [S_{\phi\psi}]\{\psi\} = \{F_\phi\} - \{F_{T\phi}\}
\end{aligned}
$$

$$(19.d)$$

$$
\begin{aligned}
&([S_{19}] + [S_{NL9}])\{s_t\} + [S_{20}]\{s_r\} + [S_{21}]\{s_{r*}\} \\
&\quad + [S_{\psi\phi}]\{\phi\} + [S_{\psi\psi}]\{\psi\} = \{F_\psi\} - \{F_{T\psi}\}
\end{aligned}
$$

$$(19.e)$$

More generally, equation (19) can be expressed as

$$[S_{eq}]\{s_t\} = \{F_{eq}\} \tag{20}$$

$[S_{eq}]$ and $\{F_{eq}\}$ denote equivalent stiffness matrix and force vector, respectively. The detailed procedure to arrive at the equations (19.a)–(19.e) and the associated stiffness matrices and force vectors are demonstrated in Appendix A and B.

## Results and discussion

The FE formulation described in the previous section is first verified for its correctness through a comparison study. To this end, the problem of nonlinear deflections of MEE plates considered by Sladek et al.[64] is resolved using the proposed formulation. A converged FE mesh of 10 × 10 is used. It can be seen in Figure 2 that there exists a close relevance between the deflection plots. Therefore, an affirmation of the credibility of the formulation is obtained. Otherwise stated, the following conditions are used for the numerical analysis:

$a/h = 50$; $a/b = 1$; Linear temperature profile; $d/l = 1$; $\theta = 20°$; $t = 1$ mm; $h/h_c = 1.4$; $t/l = 0.013857$; $E^c = 69$ GPa and $G^c = 26$ GPa.

Further, the boundary constraints used can be represented by[42]:

Clamped edge(C):
$u = v = w = \theta_x = \theta_y = \kappa_x = \kappa_y = \phi = \psi = 0$
Free edge(F):
$u = v = w = \theta_x = \theta_y = \kappa_x = \kappa_y = \phi = \psi \neq 0$
Simply supported edge(S):
$u = \theta_x = \kappa_x \neq 0; v = w = \phi = \psi = 0$ at $x = 0, a$
$v = \theta_y = \kappa_y \neq 0; u = w = \phi = \psi = 0$ at $y = 0, b$

$$(21)$$

The influence of pyro-coupling on the nonlinear deflection of sandwich plates with a different auxetic cell inclination angle is shown in Figure 3(a) and (b) for two cases of inclination angle variation. The two cases were considered because the rib lengths $l$ and $d$ are interrelated to the auxetic cell inclination angle. Altering the cell inclination angle without changing the rib lengths $l$ and $d$ was impossible. As shown in Figure 3(a), for Case-1, the inclination angle is varied, keeping the length of the inclined rib constant,
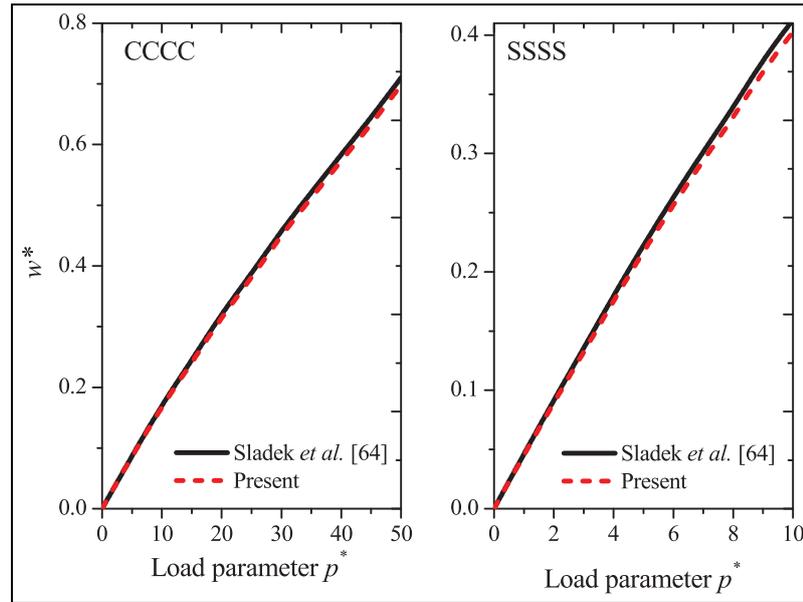
**Figure 2.** Validation of the *w*\* of three-layered MEE plate with SSSS and CCCC boundary conditions.
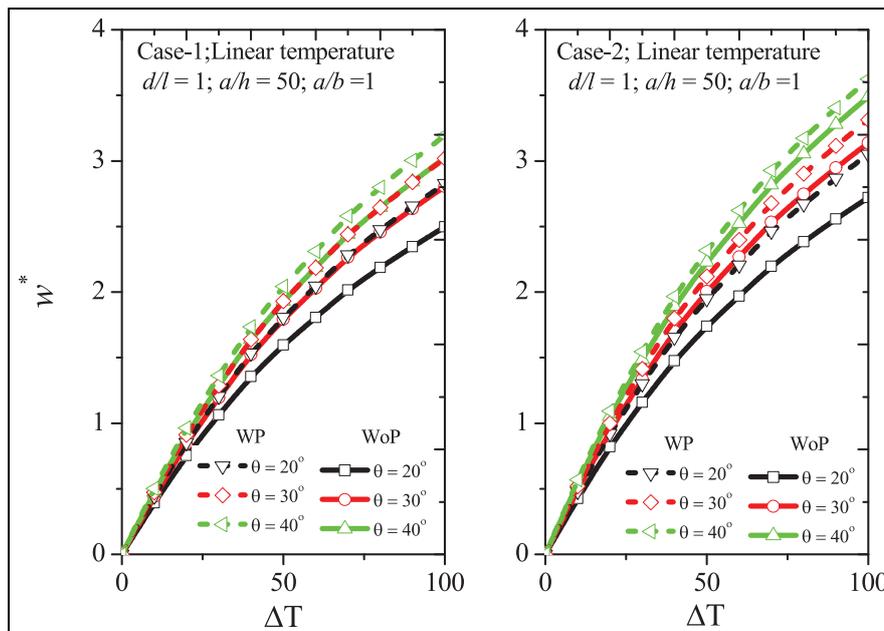


**Figure 3.** Effect of auxetic cell inclination angle and pyro-coupling on the variation of the w\* of (a) case-1 and (b) case-2 type of sandwich plate subjected to linear temperature fields.

whereas in Case-2, the length of the straight rib of the auxetic cell is kept unchanged, and the inclination angle is varied. It can be inferred from Figure 3 that increasing the unit cell inclination angle for both cases results in enhanced deflection of the sandwich plate. However, the magnitude of deflection is higher for Case-2. In addition, the pyro-coupling effects are predominant for the sandwich plates in which the auxetic cell angles are varied, keeping the length of the inclined rib constant (Case-1).

The change trends of nonlinear deflection of a sandwich plate subjected to different temperature distributions are recorded in Figure 4. As opposed to the linear temperature profile, a minimal deflection is noticed for the sandwich plate exposed to the non-linear temperature profile. Also, the effect of auxetic cell inclination angle becomes predominant when the sandwich plate is subjected to a linear temperature profile. From Figure 4(b), it can be seen that the pyro-coupling has a superior influence on the deflection when the temperature field varies linearly across the plate's thickness.

Figure 5(a) shows the relationship between the *d/l* ratio and nonlinear deflection of composite sandwich
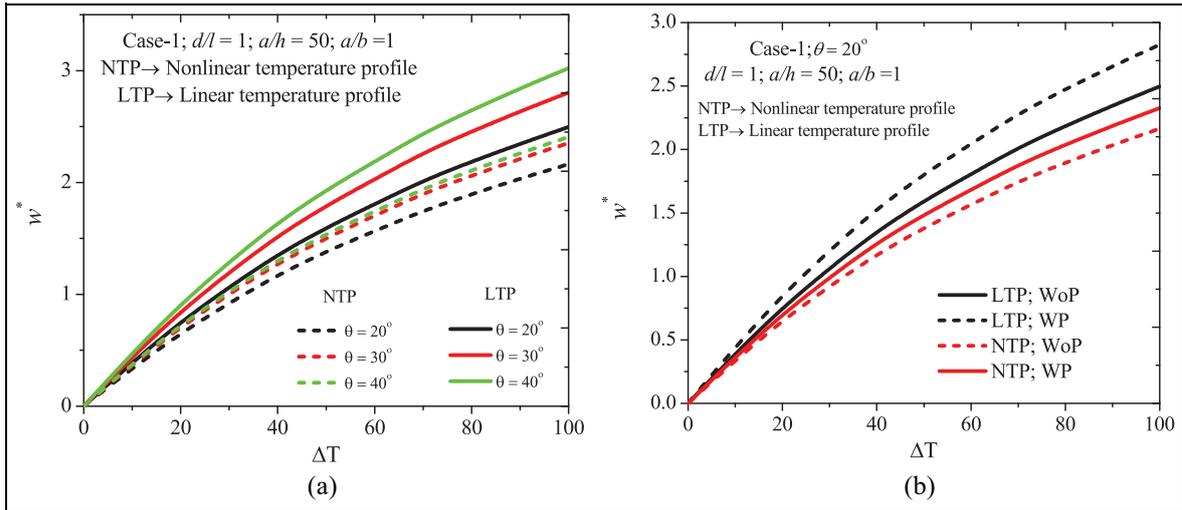
**Figure 4.** Effect of temperature profiles associated with (a) auxetic angle (b) pyro-coupling on the variation of the w* of sandwich plate.
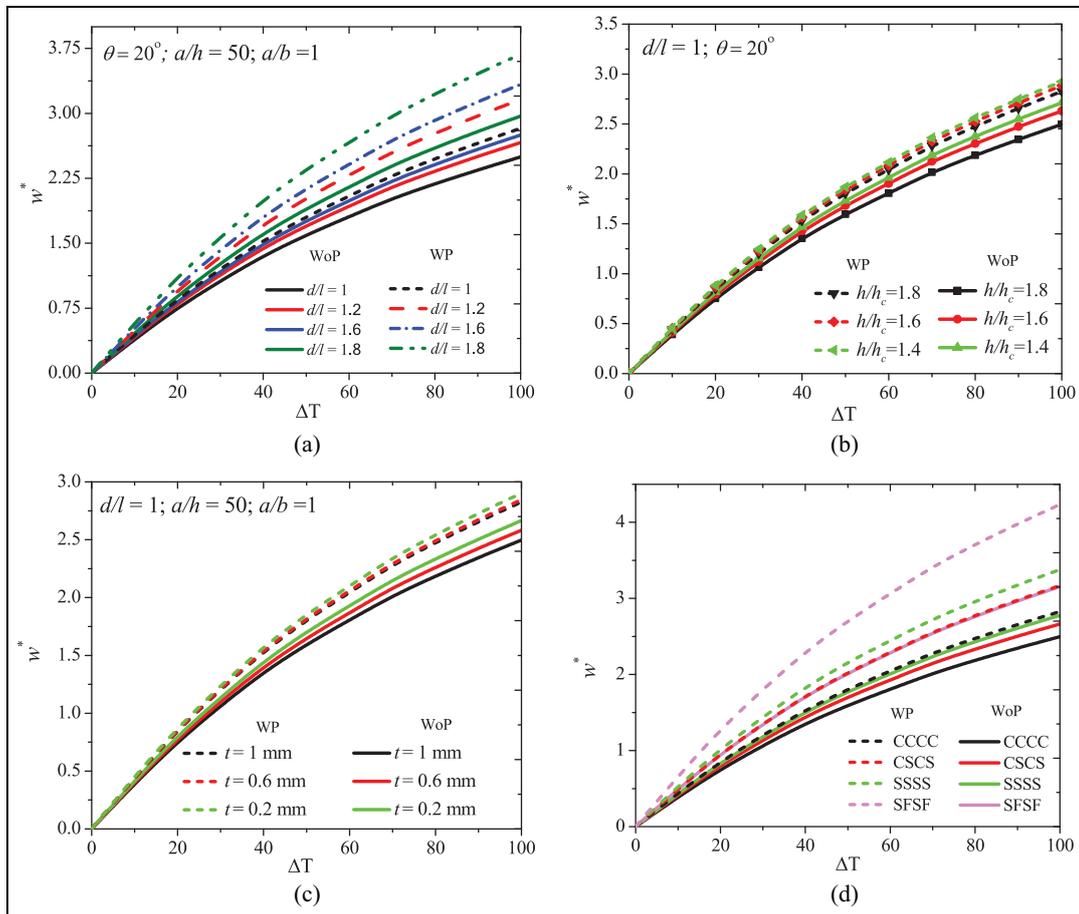


**Figure 5.** Effect of pyro-coupling associated with the: (a) *d/l* ratio, (b) h/*hc* ratio, (c) rib-thickness and (d) boundary conditions on the variation of the *w** of a sandwich plate subjected to linear temperature fields.

plates. The lower the value of *the d/l* ratio, the reduced the nonlinear deflection of the plate, indicating an improved stiffness of the plate. Furthermore, the pyro-coupling effects are minimal for a lower *d/l* ratio which can be seen through the discrepancies between the deflection curves of the plate with pyro (WP) and

without pyro-coupling (WoP). Figure 5(b) compares the deflection curves of the sandwich plate with different $h/h_c$ ratios. It can be noticed that the change trends are opposite to that of the *d/l* ratio. However, the pyro-coupling effects enhance with the greater $h/h_c$ ratio values since the volume of multifunctional
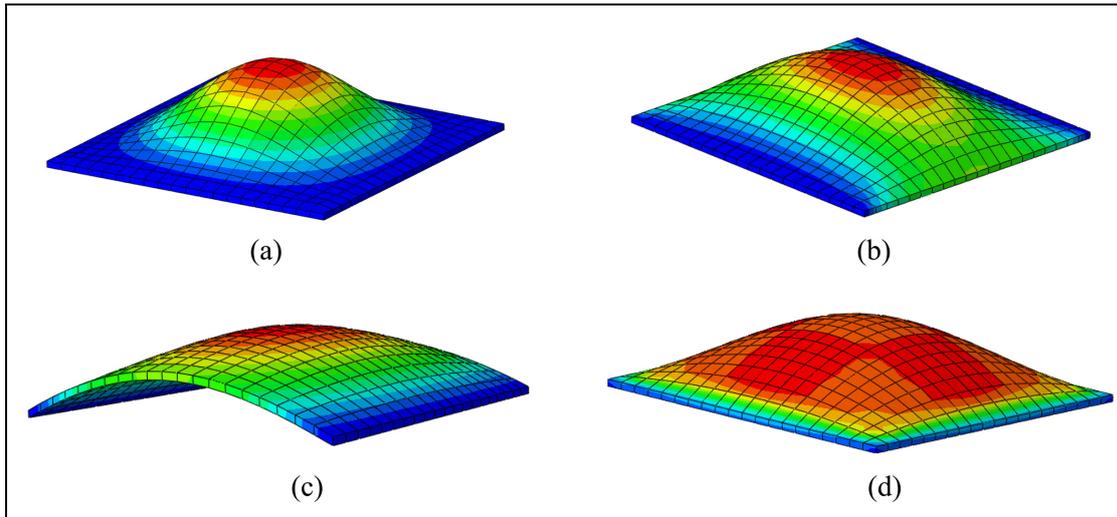
**Figure 6.** Deflection modes of the sandwich plate with different boundary conditions subjected to linear temperature profiles: (a) CCCC, (b) CSCS, (c) SFSF and (d) SSSS

**Table 2.** Effect of aspect ratio on the nonlinear deflection of sandwich plates subjected to a linear and nonlinear temperature profile ($\Delta T = 50$; $t = 1$ mm; $d/l = 1.0$; $h/h_c = 1.4$; $\theta = 20°$, $a/h = 50$).

| Temperature profile | $a/b$ | $\Delta T$ | | | | |
|---|---|---|---|---|---|---|
| | | 20 | 40 | 60 | 80 | 100 |
| Linear temperature | 1 | 0.853 | 1.534 | 2.045 | 2.475 | 2.826 |
| | 2 | 0.751 | 1.339 | 1.784 | 2.160 | 2.466 |
| | 4 | 0.578 | 1.039 | 1.384 | 1.676 | 1.913 |
| Nonlinear temperature | 1 | 0.702 | 1.263 | 1.683 | 2.038 | 2.327 |
| | 2 | 0.632 | 1.136 | 1.515 | 1.834 | 2.094 |
| | 4 | 0.514 | 0.924 | 1.232 | 1.492 | 1.703 |

**Table 3.** Effect of thickness ratio on the nonlinear deflection of sandwich plates subjected to a linear and nonlinear temperature profile ($\Delta T = 50$; $t = 1$ mm; $d/l = 1.0$; $h/h_c = 1.4$; $\theta = 20°$, $a/b = 1$).

| Temperature profile | $a/h$ | $\Delta T$ | | | | |
|---|---|---|---|---|---|---|
| | | 20 | 40 | 60 | 80 | 100 |
| Linear temperature | 10 | 0.557 | 1.002 | 1.336 | 1.617 | 1.847 |
| | 50 | 0.853 | 1.534 | 2.045 | 2.475 | 2.826 |
| | 100 | 1.469 | 2.643 | 3.523 | 4.265 | 4.870 |
| Nonlinear temperature | 10 | 0.373 | 0.672 | 0.895 | 1.084 | 1.238 |
| | 50 | 0.702 | 1.263 | 1.683 | 2.038 | 2.327 |
| | 100 | 1.044 | 1.879 | 2.504 | 3.032 | 3.461 |

MEE skins enhances, facilitating higher coupling between thermal and other fields. The effect of rib-thickness on the coupled nonlinear deflection of the sandwich plate is shown in Figure 5(c). As seen from this figure, a higher value of rib thickness results in the higher structural integrity of the plate, thereby leading to reduced deflection. Furthermore, the pyro-coupling effects are superior for the sandwich plate with higher rib-thickness. This can be attributed to the improved coupled stiffness of the overall plate. The influence of the plate's boundary conditions on its nonlinear deflection is shown in Figure 5(d). Due

to the obvious reason for improved stiffness, the sandwich plate with a higher number of clamped constraints shows a minimal deflection. The deformation shapes of the sandwich plate with different boundary conditions subjected to linear temperature rise are shown in Figure 6.

The variation of the nonlinear deflections of sandwich plates with a different aspect ratio ($a/b$) and side-to-thickness ($a/h$) ratios is presented in Tables 2 and 3, respectively. It can be witnessed from these tables that the deflections of the plate are reduced with the higher magnitude of *the $a/b$* ratio, whereas the converse holds
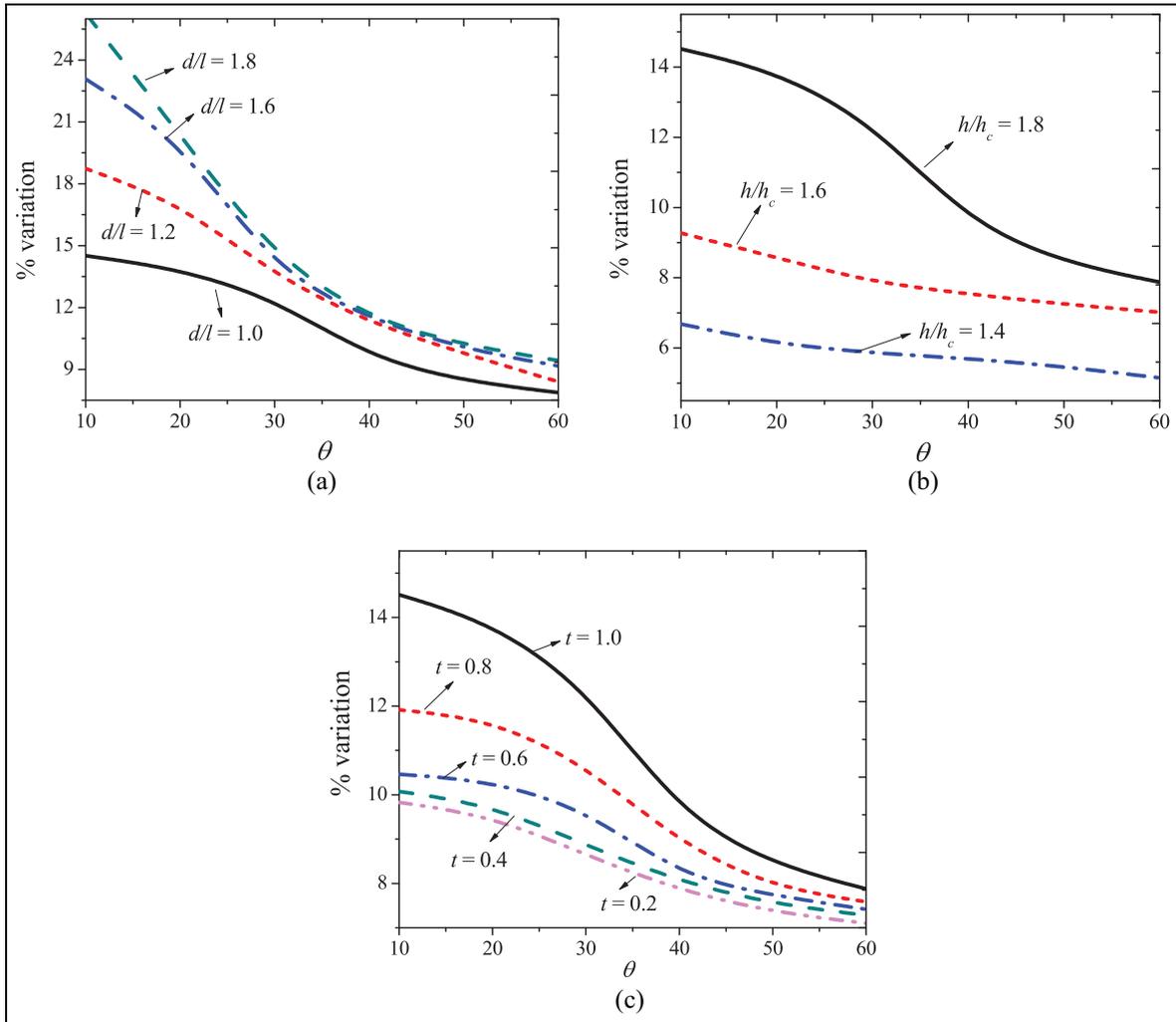
**Figure 7.** Effect of auxetic cell inclination angle on the pyro-coupling effects associated with the w* of sandwich plate with different (a) d/l ratio (b) h/hc ratio (c) rib-thickness.

good for the $a/h$ ratio. The variation in the coupled stiffness is the major reason behind these variation trends.

The synergistic effect of pyro-coupling and auxetic unit cell inclination angle on the variations in the deflections of the sandwich plate is shown in Figure 7(a) to (c). For a better understanding, the variation is sown as a percentage. It can be seen from Figure 7(a) that the influence of auxetic angle associated with the rib-length ratios ($d/l$ ratio) of the sandwich plate is predominant up to 30°. Afterwards, the discrepancies in the variation reduce. This may be due to the enhanced variation in the Poisson's ratio up to 30°, which gradually decreases later. In addition, a higher degree of variation is seen for the sandwich plate with greater values of $d/l$ ratio. Analogously, the influence of $h/h_c$ ratio and rib-thickness ($t$) associated with auxetic cell inclination angle on the variation of the pyro-coupling effects is shown in Figure 7(b) and (c), respectively. Compared with the $d/l$ ratio, a greater discrepancy in the pyro-coupling variation is witnessed for *the* $h/h_c$ ratio at higher auxetic cell

inclination angles. However, this variation is predominant at the lower inclination angles for the reasons mentioned earlier. This is due to the dominant effect of M-MEE skins over the auxetic core. The pyro-coupling effect drastically drops for lower rib-thickness values as the cell inclination angle traverses towards higher values. This may be attributed to the reduction in the coupled stiffness of the sandwich plate.

The synergistic pyro-coupling effect associated with the linear and nonlinear temperature distributions on the variation of deflections of sandwich plates is presented in Figure 8(a) to (d). The influence of different geometrical parameters is also considered here for better understanding. From these figures, it is evident that linear temperature distribution has the upper hand over the nonlinear temperature profile in terms of pyro-coupling. Further, it is also realised that a profound synergistic effect of the auxetic unit cell parameters and the temperature distributions exist on the pyro-coupling and hence the nonlinear deflections of the plate.
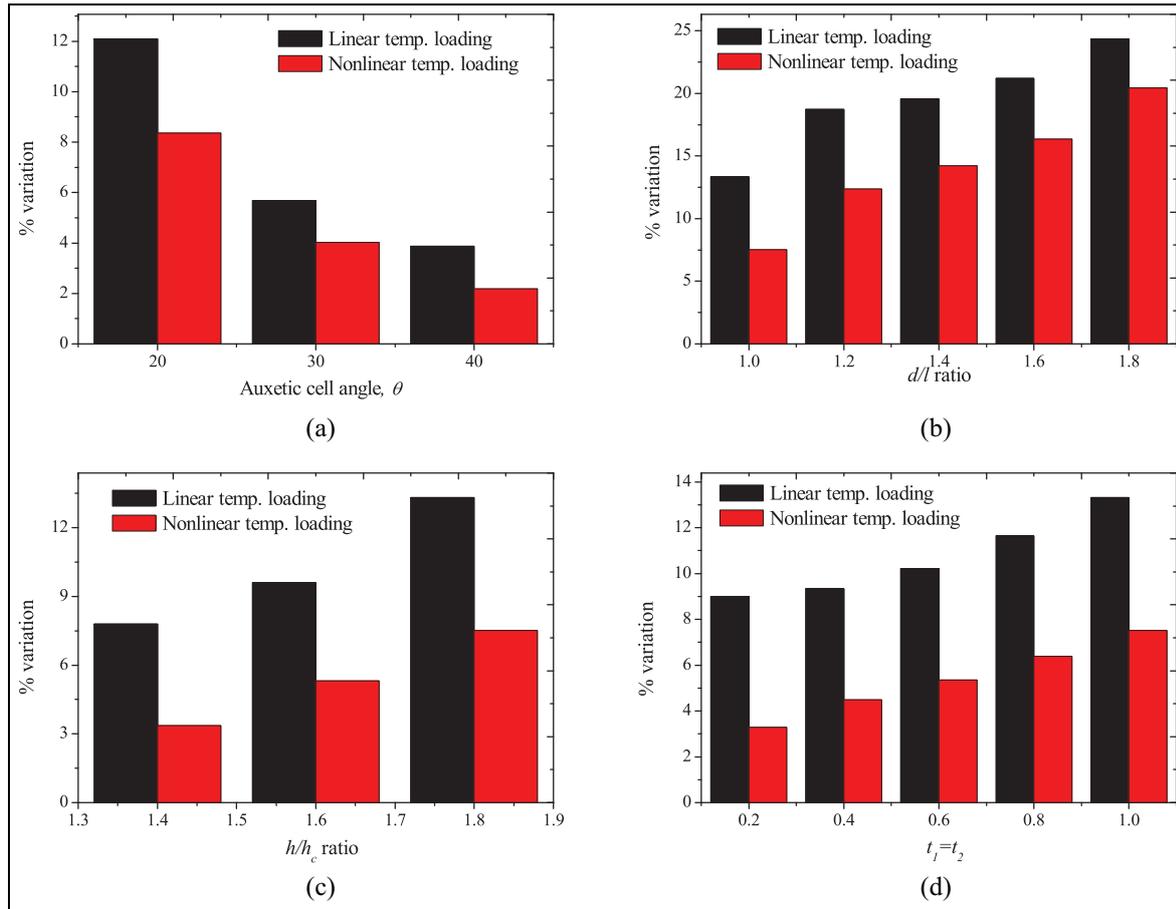
**Figure 8.** Variation of the pyro-coupling effects on the w* of a sandwich plate with different (a) auxetic angle (b) d/l ratio (c) h/hc ratio (d) rib thickness subjected to different temperature profiles.

The investigation is extended to assess the multifunctional behaviour of the sandwich plate through its bending response. The variation of the direct (electric and magnetic potentials) and indirect (electric displacement and magnetic flux densities) static quantities are examined. The influence of auxetic cell inclination angle on the distribution of static quantities is studied from Figure 9(a) to (d). Unlike the deflection response, a higher magnitude of the static quantities is noticed for a greater value of the auxetic cell inclination angle. This is due to the direct piezoelectric and magnetostriction effect of M-MEE layers. The sandwich plate with a higher auxetic cell inclination angle leads to the highest deflection, resulting in the generation of a greater magnitude of static quantities. In addition, a higher pyro-coupling effect is seen for greater auxetic cell inclination angle. A similar trend is followed for rib-length ratio and linear and nonlinear temperature profiles, as shown in Figures 10 and 11, respectively due to the obvious reasons mentioned earlier. Table 4 encapsulates the inter-related effects of various auxetic cell dimensions on the developed potentials of a sandwich plate.

The influence of applying an external electromagnetic load on the deflection and static response of

sandwich plates in a thermal environment is examined. For a sandwich plate with different auxetic cell inclination angles, increasing the positive values of electric and magnetic loads results in higher deflection of the plate as shown in Figures 12 and 13. However, the negative values tend to decrease the deflection. This is because positive electro-magnetic loads are tensile and add up to the equivalent force, but the negative electro-magnetic loads are compressive, reducing the effective force. In addition, a slightly higher influence of magnetic loads over the electric loads on the deflection can be seen. The pyro-coupling has a predominant effect on the deflection of the sandwich plate when subjected to positive electro-magnetic loads. Figures 14 and 15 show the variation of the electric and magnetic potentials, respectively, when the sandwich plate is subjected to different magnitudes of electro-magnetic loads. As seen from these figures, the negative values of the electro-magnetic loads display minimal pyro-coupling effects and reduce the generation of potentials. Further, Tables 5 and 6 show the inter-related influence of auxetic cell dimensions on the maximum potentials generated in a sandwich plate subjected to the different magnitudes of electric and magnetic
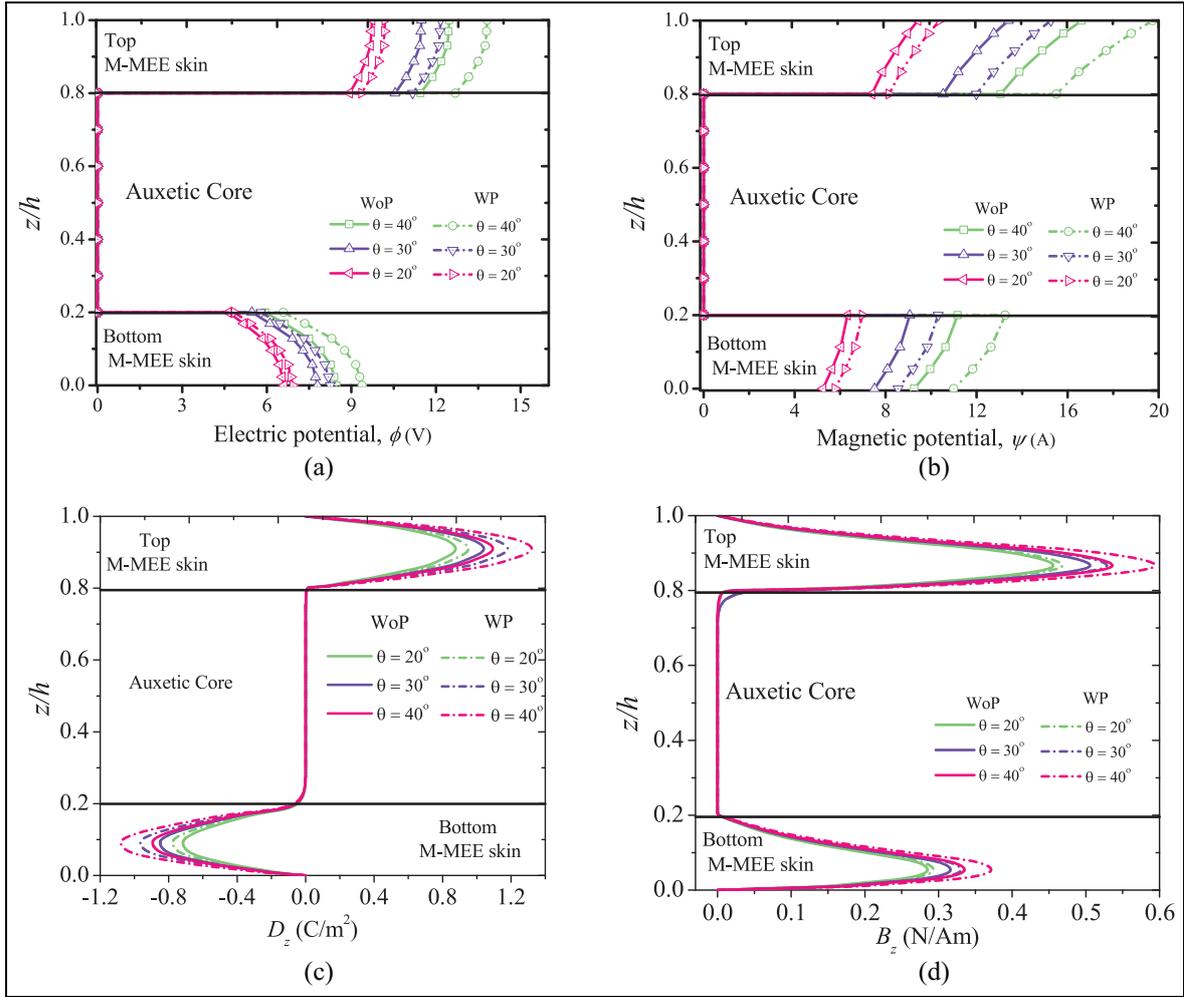
**Figure 9.** Effect of auxetic core inclination angles on the variation of the (a) electric potential (b) magnetic potential (c) electric displacement (d) magnetic flux density on the M-MEE facesheets of a sandwich plate .

**Table 4.** Effect of different auxetic cell dimensions on the maximum electric and magnetic potentials of sandwich plates subjected to a linear temperature profile ($\Delta T = 50$; $h/h_c = 1.4$).

| Rib-length ratio ($d/l$) | Rib-thickness, $t$ (mm) | Electric potential | | | Magnetic potential | | |
|---|---|---|---|---|---|---|---|
| | | $\theta = 20°$ | $\theta = 30°$ | $\theta = 40°$ | $\theta = 20°$ | $\theta = 30°$ | $\theta = 40°$ |
| $d/l = 1$ | 0.2 | 12.16 | 14.58 | 15.84 | 12.45 | 17.57 | 21.79 |
| | 0.4 | 11.31 | 13.34 | 14.49 | 11.47 | 16.32 | 20.24 |
| | 0.8 | 10.66 | 12.71 | 13.80 | 10.77 | 15.17 | 18.81 |
| | 1.0 | 9.42 | 11.48 | 12.47 | 9.73 | 13.40 | 16.62 |
| $d/l = 1.6$ | 0.2 | 14.44 | 15.42 | 16.36 | 15.86 | 20.74 | 24.43 |
| | 0.4 | 12.78 | 14.11 | 14.93 | 14.28 | 19.22 | 22.75 |
| | 0.8 | 11.38 | 13.12 | 14.01 | 12.53 | 17.72 | 20.07 |
| | 1.0 | 10.46 | 12.12 | 13.39 | 10.48 | 15.32 | 18.63 |
| $d/l = 1.8$ | 0.2 | 16.17 | 18.13 | 20.66 | 17.23 | 22.73 | 25.61 |
| | 0.4 | 13.52 | 16.42 | 17.55 | 15.84 | 21.12 | 23.68 |
| | 0.8 | 12.26 | 14.98 | 15.69 | 13.83 | 19.27 | 21.92 |
| | 1.0 | 10.80 | 13.18 | 14.77 | 10.95 | 17.18 | 20.33 |
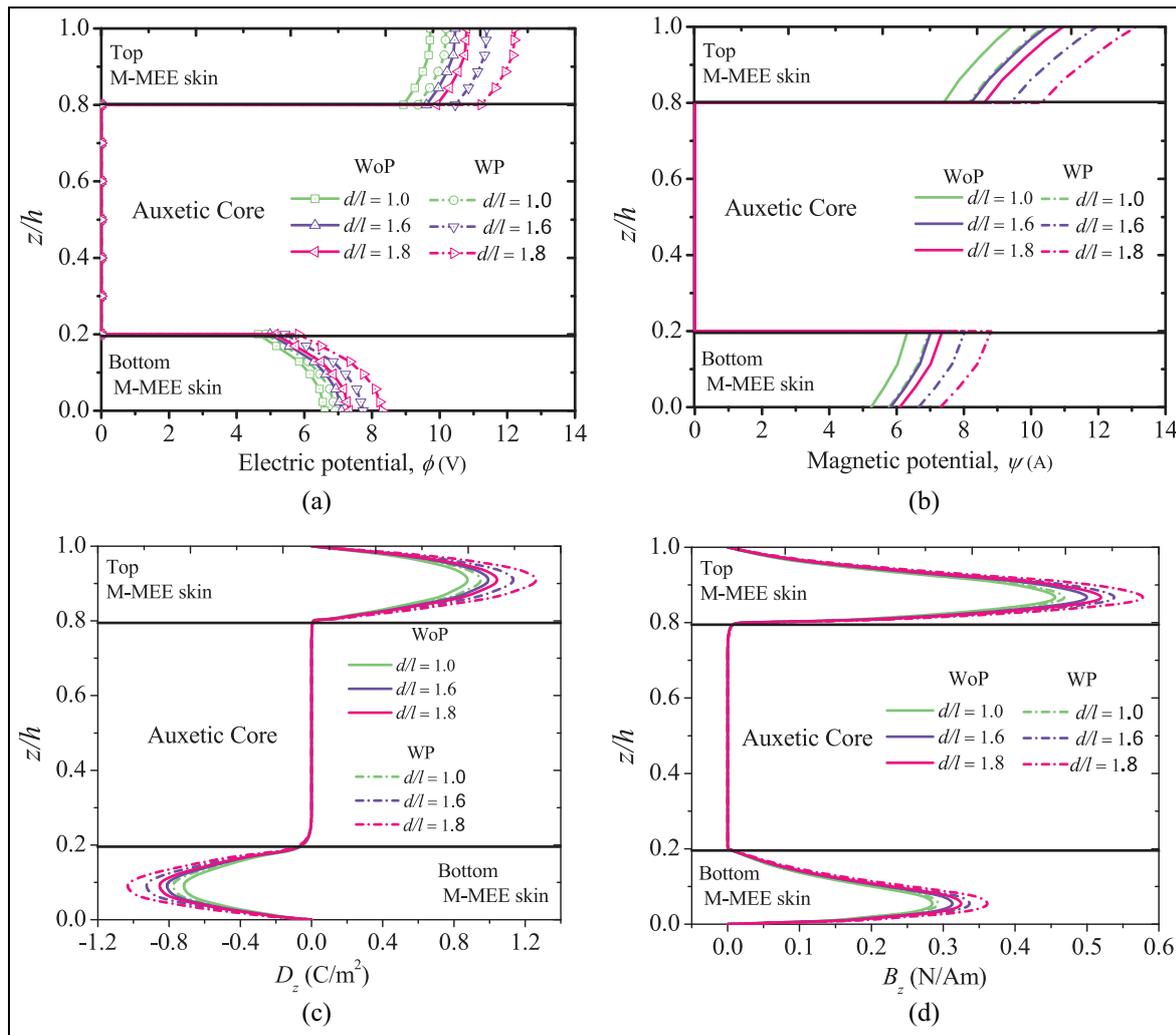
**Figure 10.** Effect of rib-length ratios on the variation of the: (a) electric potential, (b) magnetic potential, (c) electric displacement and (d) magnetic flux density on the M-MEE facesheets of a sandwich plate.

loads. It can be witnessed that magnetic loads have a significant effect on the potentials due to higher magnetic coupling coefficients.

## Conclusions

In this research work, the sandwich plate's nonlinear deflection and bending response with auxetic core and M-MEE skins subjected to the multi-physics loads (electric, magnetic and thermal) are studied. The emphasis has been made on studying the inter-related effects of auxeticity of the core, multi-physics loads and pyro-coupling characteristics of the smart skin. A mathematical model reinforced with the higher order shear deformation theory, and von-Karman's nonlinearity is presented using the FE framework. The numerical examples suggest that the pyro-coupling and auxeticity effects are interrelated and jointly dictate the nonlinear deflection of the sandwich plate. In other words, the degree of pyro-coupling can be varied by controlling the geometric

parameters of the auxetic unit cells. Few of the prominent outcomes of this work suggest that the linear temperature profile significantly affects the deflections more than the nonlinear temperature profile. The significant influence of temperature profiles on the pyro-coupling are witnessed at lower auxetic cell angle. A variation of 3.77% with respect to the pyro-coupling effect exists between the linear and nonlinear thermal profiles when $\theta = 20°$. Lower values of rib-thickness and plate-to-auxetic core thickness ratio result in an enhanced pyro-coupling effect, whereas a predominant effect of a higher rib-length ratio is seen on the pyro-coupling. However, due to the direct piezoelectric and piezomagnetic properties of M-MEE skin, a higher auxetic cell inclination angle and the rib-length ratio has a beneficial effect on the development of potentials. The electric and magnetic potentials developed tend to improve by 32.97% and 38.39% rib-length ratio is varied from 1 to 1.8. Therefore, it is evident from this study that mainly by controlling the auxetic cell parameters, the smart sensing and
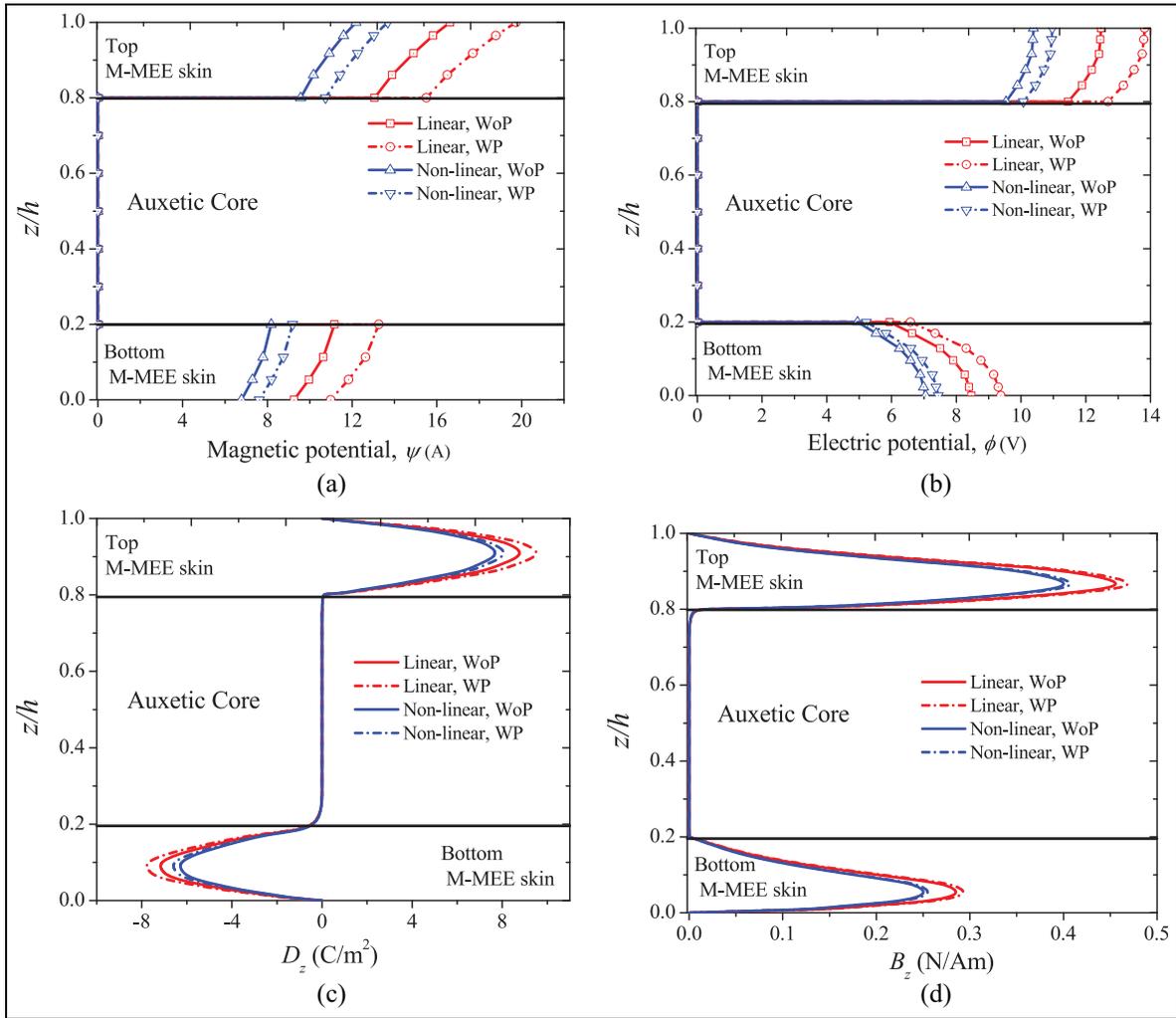
**Figure 11.** Effect of temperature profiles on the variation of the: (a) electric potential, (b) magnetic potential, (c) electric displacement and (d) magnetic flux density on the top and bottom M-MEE facesheets of a sandwich plate.
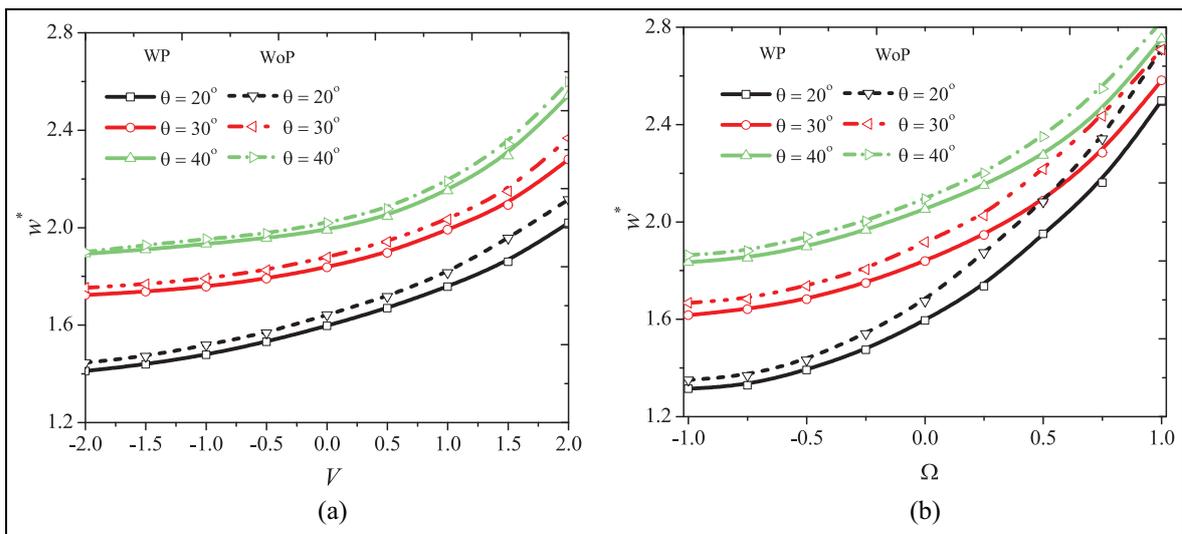


**Figure 12.** Effect of: (a) electric and (b) magnetic loads on the nonlinear deflections of a sandwich plate with different auxetic inclination angle.
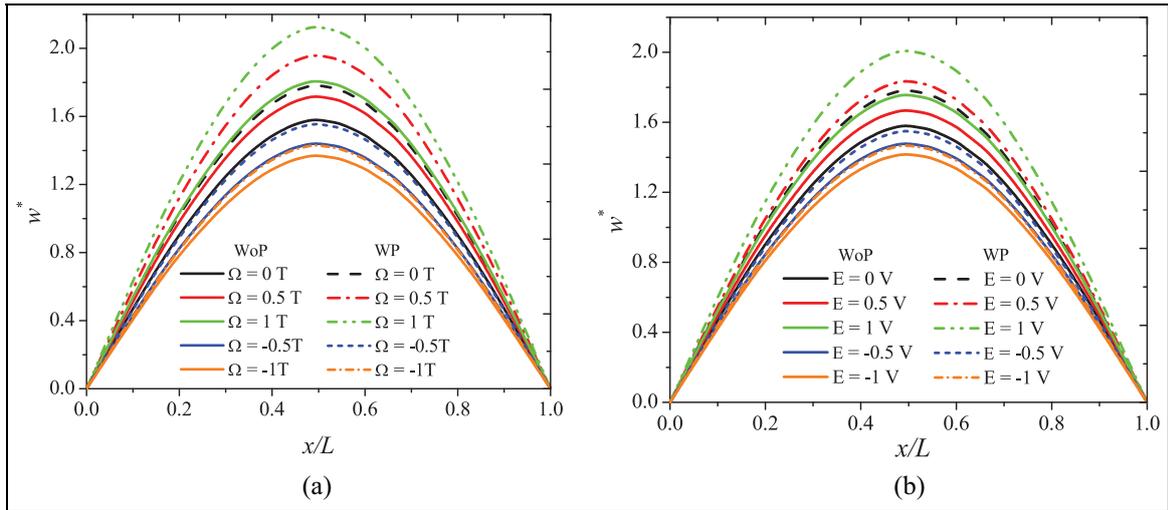
**Figure 13.** Effect of pyro-coupling on the centre deflections of a sandwich plate subjected to different magnitudes of: (a) electric and (b) magnetic loads along with linear thermal loads.
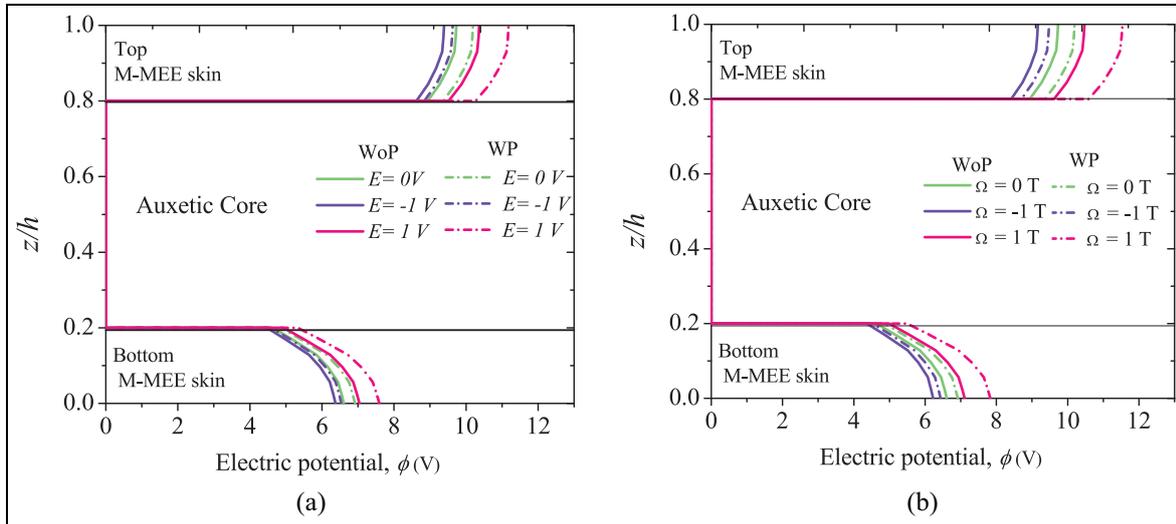


**Figure 14.** Variation of the electric potential across a sandwich plate subjected to: (a) electric and (b) magnetic loads.
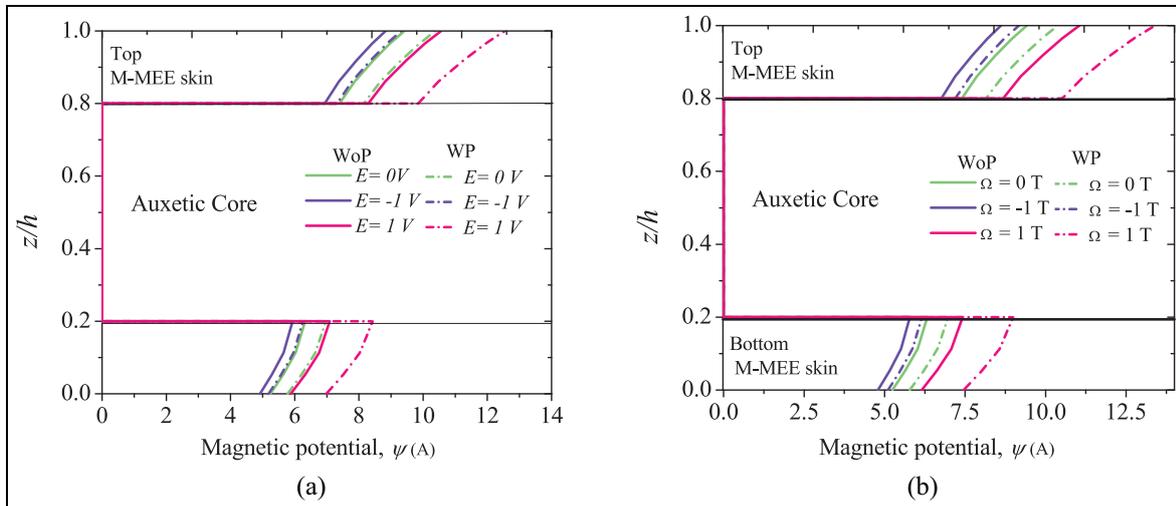


**Figure 15.** Variation of the magnetic potential across a sandwich plate subjected to: (a) electric and (b) magnetic loads.

**Table 5.** Effect of electric loads on the maximum electric and magnetic potentials of sandwich plates subjected to a linear temperature profile ($\Delta T = 50$; $t = 1$ mm; $h/h_c = 1.4$).

| Rib-length ratio ($d/l$) | Electric load (V) | Electric potential (V) | | | Magnetic potential (A) | | |
|---|---|---|---|---|---|---|---|
| | | $\theta = 20°$ | $\theta = 30°$ | $\theta = 40°$ | $\theta = 20°$ | $\theta = 30°$ | $\theta = 40°$ |
| $d/l = 1$ | −1 | 8.72 | 9.10 | 9.88 | 8.44 | 9.27 | 10.07 |
| | −0.5 | 9.11 | 10.16 | 11.54 | 9.03 | 10.34 | 12.53 |
| | 0 | 9.42 | 11.48 | 12.47 | 9.73 | 13.40 | 16.62 |
| | 0.5 | 9.95 | 12.05 | 13.18 | 10.12 | 14.66 | 17.37 |
| | 1.0 | 10.36 | 12.97 | 14.43 | 10.91 | 16.38 | 18.32 |
| $d/l = 1.6$ | −1 | 9.08 | 9.72 | 10.33 | 9.17 | 9.92 | 12.70 |
| | −0.5 | 9.79 | 11.38 | 12.26 | 9.86 | 12.89 | 16.52 |
| | 0 | 10.46 | 12.12 | 13.39 | 10.48 | 15.32 | 18.63 |
| | 0.5 | 10.98 | 13.66 | 14.76 | 11.11 | 16.41 | 19.33 |
| | 1.0 | 11.56 | 14.92 | 15.88 | 12.54 | 17.82 | 20.05 |
| $d/l = 1.8$ | −1 | 9.64 | 10.17 | 11.12 | 9.78 | 12.82 | 14.27 |
| | −0.5 | 10.11 | 12.43 | 13.73 | 10.28 | 15.56 | 17.92 |
| | 0 | 10.80 | 13.18 | 14.77 | 10.95 | 17.18 | 20.33 |
| | 0.5 | 11.59 | 15.32 | 16.65 | 12.25 | 18.27 | 21.66 |
| | 1.0 | 12.11 | 16.77 | 18.54 | 14.22 | 19.49 | 23.82 |

**Table 6.** Effect of magnetic loads on the maximum electric and magnetic potentials of sandwich plates subjected to a linear temperature profile ($\Delta T = 50$; $t = 1$ mm; $h/h_c = 1.4$).

| Rib-length ratio ($d/l$) | Magnetic load (T) | Electric potential | | | Magnetic potential | | |
|---|---|---|---|---|---|---|---|
| | | $\theta = 20°$ | $\theta = 30°$ | $\theta = 40°$ | $\theta = 20°$ | $\theta = 30°$ | $\theta = 40°$ |
| $d/l = 1$ | −1 | 8.03 | 8.38 | 9.10 | 7.77 | 8.54 | 9.27 |
| | −0.5 | 8.39 | 9.36 | 10.63 | 8.32 | 9.52 | 11.54 |
| | 0 | 9.42 | 11.48 | 12.47 | 9.73 | 13.40 | 16.62 |
| | 0.5 | 10.27 | 12.44 | 13.60 | 10.44 | 15.13 | 17.93 |
| | 1.0 | 10.69 | 13.39 | 14.89 | 11.26 | 16.90 | 18.91 |
| $d/l = 1.6$ | −1 | 8.48 | 9.08 | 9.65 | 8.56 | 9.27 | 11.86 |
| | −0.5 | 9.14 | 10.63 | 11.45 | 9.21 | 12.04 | 15.43 |
| | 0 | 10.46 | 12.12 | 13.39 | 10.48 | 15.32 | 18.63 |
| | 0.5 | 11.58 | 14.41 | 15.57 | 11.72 | 17.31 | 20.39 |
| | 1.0 | 12.20 | 15.74 | 16.75 | 13.23 | 18.80 | 21.15 |
| $d/l = 1.8$ | −1 | 9.18 | 9.68 | 10.59 | 9.31 | 12.20 | 13.59 |
| | −0.5 | 9.62 | 11.83 | 13.07 | 9.79 | 14.81 | 17.06 |
| | 0 | 10.80 | 13.18 | 14.77 | 10.95 | 17.18 | 20.33 |
| | 0.5 | 12.49 | 16.51 | 17.94 | 13.20 | 19.69 | 23.34 |
| | 1.0 | 13.05 | 18.07 | 19.98 | 15.32 | 21.00 | 25.67 |

actuation capabilities of the structures can be altered. The prominent outcomes of this work related to integrated effects of auxeticity and pyro-coupling are not yet reported in the open literature and are deemed to be utilised as a future reference.

## ORCID iD

Vinyas Mahesh https://orcid.org/0000-0001-8394-1321

## Data availability

The raw/processed data required to reproduce these findings cannot be shared at this time as the data also forms part of an ongoing study.

## References

1. Brighenti R, Spagnoli A, Lanfranchi M, et al. Non-linear deformation behaviour of auxetic cellular

materials with re-entrant lattice structure. *Fatigue Fract Eng Mater Struct* 2016; 39(5): 599–610.

2. Hou Y, Tai YH, Lira C, et al. The bending and failure of sandwich structures with auxetic gradient cellular cores. *Compos Part A Appl Sci Manuf* 2013; 49: 119–131.

3. Jin X, Wang Z, Ning J, et al. Dynamic response of sandwich structures with graded auxetic honeycomb cores under blast loading. *Compos B Eng* 2016; 106: 206–217.

4. Li C, Shen HS and Wang H. Nonlinear bending of sandwich beams with functionally graded negative Poisson's ratio honeycomb core. *Compos Struct* 2019; 212: 317–325.

5. Boldrin L, Hummel S, Scarpa F, et al. Dynamic behaviour of auxetic gradient composite hexagonal honeycombs. *Compos Struct* 2016; 149: 114–124.

6. Li C, Shen HS and Wang H. Thermal post-buckling of sandwich beams with functionally graded negative Poisson's ratio honeycomb core. *Int J Mech Sci* 2019; 152: 289–297.

7. Li C, Shen HS and Wang H. Nonlinear dynamic response of sandwich beams with functionally graded negative Poisson's ratio honeycomb core. *Eur Phys J Plus* 2019; 134(2): 1–15.

8. Bendenia N, Zidour M, Bousahla AA, et al. Deflections, stresses and free vibration studies of FG-CNT reinforced sandwich plates resting on Pasternak elastic foundation. *Comput Concr* 2020; 26(3): 213–226.

9. Allam O, Draiche K, Bousahla AA, et al. A generalized 4-unknown refined theory for bending and free vibration analysis of laminated composite and sandwich plates and shells. *Comput Concr* 2020; 26(2): 185–201.

10. Menasria A, Kaci A, Bousahla AA, et al. A four-unknown refined plate theory for dynamic analysis of FG-sandwich plates under various boundary conditions. *Steel Compos Struct* 2020; 36(3): 355–367.

11. Zaitoun MW, Chikh A, Tounsi A, et al. An efficient computational model for vibration behavior of a functionally graded sandwich plate in a hygrothermal environment with viscoelastic foundation effects. *Eng Comput* 2021; 1–15. https://doi.org/10.1007/s00366-021-01498-1

12. Zaitoun MW, Chikh A, Tounsi A, et al. Influence of the visco-Pasternak foundation parameters on the buckling behavior of a sandwich functional graded ceramic–metal plate in a hygrothermal environment. *Thin-Walled Struct* 2022; 170: 108549.

13. Tahir SI, Chikh A, Tounsi A, et al. Wave propagation analysis of a ceramic-metal functionally graded sandwich plate with different porosity distributions in a hygro-thermal environment. *Compos Struct* 2021; 269: 114030.

14. Kong F, Dong F, Duan M, et al. On the vibrations of the electrorheological sandwich disk with composite face sheets considering pre and post-yield regions. *Thin-Walled Struct* 2022; 179: 109631.

15. Tahir SI, Tounsi A, Chikh A, et al. The effect of three-variable viscoelastic foundation on the wave propagation in functionally graded sandwich plates via a simple quasi-3D HSDT. *Steel Compos Struct* 2022; 42(4): 501.

16. Vinyas M. Computational analysis of smart magneto-electro-elastic materials and structures: review and classification. *Arch Comput Methods Eng* 2021; 28(3): 1205–1248.

17. Mahesh V. Nonlinear damping of auxetic sandwich plates with functionally graded magneto-electro-elastic facings under multiphysics loads and electromagnetic circuits. *Compos Struct* 2022; 290: 115523.

18. Mahesh V. Active control of nonlinear coupled transient vibrations of multifunctional sandwich plates with agglomerated FG-CNTs core/magneto-electro-elastic facesheets. *Thin-Walled Struct* 2022; 179: 109547.

19. Mahesh V and Ponnusami SA. Nonlinear damped transient response of sandwich auxetic plates with porous magneto-electro-elastic facesheets. *Eur Phys J Plus* 2022; 137(5): 1–21.

20. Mahesh V. Nonlinear damped transient vibrations of carbon nanotube-reinforced magneto-electro-elastic shells with different electromagnetic circuits. *J Vib Eng Technol* 2022; 10(1): 351–374.

21. Vinyas M, Harursampath D and Nguyen-Thoi T. Influence of active constrained layer damping on the coupled vibration response of functionally graded magneto-electro-elastic plates with skewed edges. *Def Technol* 2020; 16(5): 1019–1038.

22. Vinyas M. Interphase effect on the controlled frequency response of three-phase smart magneto-electro-elastic plates embedded with active constrained layer damping: FE study. *Mater Res Express* 2020; 6(12): 125707.

23. Vinyas M. Vibration control of skew magneto-electro-elastic plates using active constrained layer damping. *Compos Struct* 2019; 208: 600–617.

24. Siddharth Mangalasseri A, Mahesh V, Mahesh V, et al. Investigation on the interphase effects on the energy harvesting characteristics of three phase magneto-electro-elastic cantilever beam. *Mech Adv Mater Struct* 2022; 1–13. https://doi.org/10.1080/15376494.2022.2062630

25. Mangalasseri AS, Mahesh V, Mukunda S, et al. Vibration-based energy harvesting characteristics of functionally graded magneto-electro-elastic beam structures using lumped parameter model. *J Vib Eng Technol* 2022; 10: 1705–1720.

26. Mahesh V. Porosity effect on the energy harvesting behaviour of functionally graded magneto-electro-elastic/fibre-reinforced composite beam. *Eur Phys J Plus* 2022; 137(1): 1–39.

27. Mahesh V and Mangalasseri AS. Agglomeration effects of CNTs on the energy harvesting performance of multifield interactive magneto-electro-elastic/nanocomposite unimorph smart beam. Mech Based Des Struct Mach 2022; 1–27. https://doi.org/10.1080/15397734.2022.2144886

28. Mahesh V, Mahesh V, Mukunda S, et al. Influence of micro-topological textures of $BaTiO_3$–$CoFe_2O_4$ composites on the nonlinear pyrocoupled dynamic response of blast loaded magneto-electro-elastic plates in thermal environment. *Eur Phys J Plus* 2022; 137(6): 1–22.

29. Mahesh V. A numerical investigation on the nonlinear pyrocoupled dynamic response of blast loaded magnetoelectroelastic multiphase porous plates in thermal environment. *Eur Phys J Plus* 2022; 137(5): 1–24.

30. Mahesh V. Nonlinear pyrocoupled dynamic response of functionally graded magnetoelectroelastic plates under blast loading in thermal environment. *Mech Based Des Struct Mach* 2022; 1–26. https://doi.org/10.1080/15397734.2022.2047723

31. Zhao YF, Zhang SQ, Wang X, et al. Nonlinear analysis of carbon nanotube reinforced functionally graded

plates with magneto-electro-elastic multiphase matrix. *Compos Struct* 2022; 297: 115969.

32. Zhou L, Wang J, Li X, et al. The magneto-electro-elastic multi-physics coupling element free Galerkin method for smart structures in statics and dynamics problems. *Thin-Walled Struct* 2021; 169: 108431.

33. Quang VD, Quan TQ and Tran P. Static buckling analysis and geometrical optimization of magneto-electro-elastic sandwich plate with auxetic honeycomb core. *Thin-Walled Struct* 2022; 173: 108935.

34. Dinh Dat N, Quoc Quan T and Dinh Duc N. Vibration analysis of auxetic laminated plate with magneto-electro-elastic face sheets subjected to blast loading. *Compos Struct* 2022; 280: 114925.

35. Nie B, Meng G, Ren S, et al. Stable node-based smoothed radial point interpolation method for the dynamic analysis of the hygro-thermo-magneto-electro-elastic coupling problem. *Eng Anal Bound Elem* 2022; 134: 435–452.

36. Vinyas M and Kattimani SC. Static analysis of stepped functionally graded magneto-electro-elastic plates in thermal environment: a finite element study. *Compos Struct* 2017; 178: 63–86.

37. Vinyas M and Kattimani SC. Static studies of stepped functionally graded magneto-electro-elastic beam subjected to different thermal loads. *Compos Struct* 2017; 163: 216–237.

38. Vinyas M, Kattimani SC, Loja MAR, et al. Effect of $BaTiO_3/CoFe_2O_4$ micro-topological textures on the coupled static behaviour of magneto-electro-thermo-elastic beams in different thermal environment. *Mater Res Express* 2018; 5(12): 125702.

39. Vinyas M, Harursampath D and Kattimani SC. Thermal response analysis of multi-layered magneto-electro-thermo-elastic plates using higher order shear deformation theory. *Struct Eng Mech* 2020; 73(6): 667–684.

40. Mahesh V. Nonlinear deflection of carbon nanotube reinforced multiphase magneto-electro-elastic plates in thermal environment considering pyrocoupling effects. *Math Methods Appl Sci* 2020. https://doi.org/10.1002/mma.6858

41. Mahesh V. Nonlinear pyrocoupled deflection of viscoelastic sandwich shell with CNT reinforced magneto-electro-elastic facing subjected to electromagnetic loads in thermal environment. *Eur Phys J Plus* 2021; 136(8): 1–30.

42. Mahesh V. Effect of carbon nanotube-reinforced magneto-electro-elastic facings on the pyrocoupled nonlinear deflection of viscoelastic sandwich skew plates in thermal environment. *Proc IMechE Part L: J Materials Design Applications* 2022; 236(1): 200–221.

43. Hirwani CK and Panda SK. Nonlinear finite element solutions of thermoelastic deflection and stress responses of internally damaged curved panel structure. *Appl Math Model* 2019; 65: 303–317.

44. Chen CF and Chen JH. Nonlinear study of large deflection of simply supported piezoelectric layered-plate under initial tension. *Int J Mech Sci* 2011; 53(7): 485–493.

45. Zhang LW, Lei ZX, Liew KM, et al. Large deflection geometrically nonlinear analysis of carbon nanotube-reinforced functionally graded cylindrical panels. *Comput Methods Appl Mech Eng* 2014; 273: 1–18.

46. Alamatian J and Golmakani ME. Large deflection analysis of the moderately thick general theta ply

laminated plates on nonlinear elastic foundation with various boundary conditions. *Mech Res Commun* 2013; 51: 78–85.

47. Sepahi O, Forouzan MR and Malekzadeh P. Large deflection analysis of thermo-mechanical loaded annular FGM plates on nonlinear elastic foundation via DQM. *Compos Struct* 2010; 92(10): 2369–2378.

48. Tiar A, Zouari W, Kebir H, et al. A nonlinear finite element formulation for large deflection analysis of 2D composite structures. *Compos Struct* 2016; 153: 262–270.

49. Mehar K and Panda SK. Numerical investigation of nonlinear thermomechanical deflection of functionally graded CNT reinforced doubly curved composite shell panel under different mechanical loads. *Compos Struct* 2017; 161: 287–298.

50. Gholami R and Ansari R. Large deflection geometrically nonlinear analysis of functionally graded multi-layer graphene platelet-reinforced polymer composite rectangular plates. *Compos Struct* 2017; 180: 760–771.

51. Mareishi S, Rafiee M, He XQ, et al. Nonlinear free vibration, postbuckling and nonlinear static deflection of piezoelectric fiber-reinforced laminated composite beams. *Compos B Eng* 2014; 59: 123–132.

52. Sh EL, Kattimani S and Vinyas M. Nonlinear free vibration and transient responses of porous functionally graded magneto-electro-elastic plates. *Arch Civil Mech Eng* 2022; 22(1): 1–26.

53. Mahesh V and Harursampath D. Large deflection analysis of functionally graded magneto-electro-elastic porous flat panels. *Eng Comput* 2022; 38(S2): 1615–1634.

54. Quan TQ, Anh VM, Mahesh V, et al. Vibration and nonlinear dynamic response of imperfect sandwich piezoelectric auxetic plate. *Mech Adv Mater Struct* 2022; 29(1): 127–137.

55. Mahesh V, Mahesh V, Harursampath D, et al. Simulation-based assessment of coupled frequency response of magneto-electro-elastic auxetic multifunctional structures subjected to various electromagnetic circuits. *Proc IMechE Part L: J Materials Design Applications* 2022; 236: 2281–2296.

56. Mahesh V and Harursampath D. Nonlinear deflection analysis of CNT/magneto-electro-elastic smart shells under multi-physics loading. *Mech Adv Mater Struct* 2022; 29(7): 1047–1071.

57. Mahesh V. Nonlinear free vibration of multifunctional sandwich plates with auxetic core and magneto-electro-elastic facesheets of different micro-topological textures: FE approach. *Mech Adv Mater Struct* 2022; 29: 6266–6287.

58. Van Vinh P, Van Chinh N and Tounsi A. Static bending and buckling analysis of bi-directional functionally graded porous plates using an improved first-order shear deformation theory and FEM. *Eur J Mech A/Solids* 2022; 96: 104743.

59. Garg A, Belarbi MO, Tounsi A, et al. Predicting elemental stiffness matrix of FG nanoplates using Gaussian process regression based surrogate model in framework of layerwise model. *Eng Anal Bound Elem* 2022; 143: 779–795.

60. Kumar Y, Gupta A and Tounsi A. Size-dependent vibration response of porous graded nanostructure with FEM and nonlocal continuum model. *Adv Nano Res* 2021; 11(1): 1–17.

61. Alimirzaei S, Mohammadimehr M and Tounsi A. Nonlinear analysis of viscoelastic micro-composite beam with geometrical imperfection using FEM: MSGT electro-magneto-elastic bending, buckling and vibration solutions. *Struct Eng Mech* 2019; 71(5): 485–502.
62. Zenkour AM and Sobhy M. Thermal buckling of various types of FGM sandwich plates. *Compos Struct* 2010; 93(1): 93–102.
63. Reddy JN. *An introduction to nonlinear finite element analysis with applications to heat transfer, fluid mechanics, and solid mechanics*. 2nd ed. Cambridge: Oxford University Press, 2004.
64. Sladek J, Sladek V, Krahulec S, et al. The MLPG analyses of large deflections of magnetoelectroelastic plates. *Eng Anal Bound Elem* 2013; 37(4): 673–682.

## Appendix A

To derive, equation (20), the previous equations are condensed based on the d.o.f's as shown:

The equation (19.e), is solved in a direct manner to obtain $\{\psi\}$ as follows:

$$\{\psi\} = -\left[S_{\psi\eta\psi}\right]^{-1}$$
$$\left\{\begin{array}{l}([S_{19}] + [S_{NL9}])\{d_t\} + [S_{20}]\{d_r\} + [S_{21}]\{d_{r*}\} + \\ [S_{\phi\psi}]^T\{\phi\} - \{F_\psi\} + \{F_{T\psi}\}\end{array}\right\}$$
$$(A.1)$$

The term $\{\psi\}$ of equation (19.d) is substituted by the equation (A.1) and solved for $\{\phi\}$ to get,

$$([S_{16}] + [S_{NL8}])\{d_t\} + [S_{17}]\{d_r\} + [S_{18}]\{d_{r*}\} + [S_{\phi\phi}]\{\phi\} -$$
$$[S_{\phi\psi}]\left[[S_{\psi\eta\psi}]^{-1}\left(\begin{array}{l}([S_{19}] + [S_{NL9}])\{s_t\} + [S_{20}]\{s_r\} + [S_{21}]\{s_{r*}\} + \\ [S_{\phi\psi}]^T\{\phi\} - \{F_\psi\} + \{F_{T\psi}\}\end{array}\right)\right]$$
$$= \{F_\phi\} - \{F_{T\phi}\}$$
$$([S_{22}] + [S_{NL11}])\{s_t\} + [S_{23}]\{s_r\} + [S_{24}]\{s_{r*}\} + [S_{25}]\{\phi\}$$
$$+ [S_{\phi\phi}][S_{\psi\eta\psi}]^{-1}(\{F_\psi\} - \{F_{T\psi}\}) = (\{F_\phi\} - \{F_{T\phi}\})$$
$$\{\phi\} = \left(\begin{array}{l}-[S_{26}]\{s_t\} - [S_{NL\_12}]\{s_t\} - [S_{27}]\{s_r\} - [S_{28}]\{s_{r*}\} - \\ [S_{F1}](\{F_\psi\} - \{F_{t\psi}\}) - [S_{25}]^{-1}(\{F_\phi\} - \{F_{t\phi}\})\end{array}\right)$$
$$(A.2)$$

Likewise, the terms $\{\psi\}$ and $\{\varphi\}$ of equation (19.c) is replaced with the equations (A.1) and (A.2) and solved for $\{s_{r*}\}$, to deduce

$$([S_{29}] + [S_{NL13}])\{s_t\} + [S_{30}]\{s_r\} + [S_{31}]\{s_{r*}\} + [S_{32}]\{\phi\}$$
$$+ [S_{F2}](\{F_\psi\} - \{F_{T\psi}\}) = 0$$
$$([S_{33}] + [S_{NL15}])\{s_t\} + [S_{34}]\{s_r\} + [S_{35}]\{s_{r*}\} +$$
$$+ [S_{F5}](\{F_\psi\} - \{F_{T\psi}\}) - [K_{F3}](\{F_\phi\} - \{F_{T\phi}\}) = 0$$
$$\{s_{r*}\} = \left(\begin{array}{l}-[S_{36}]\{s_t\} - [S_{NL\_16}]\{s_t\} - [S_{37}]\{s_r\} - \\ [S_{F6}](\{F_\psi\} - \{F_{T\psi}\}) - [S_{F7}](\{F_\phi\} - \{F_{T\phi}\})\end{array}\right)$$
$$(A.3)$$

In a similar fashion, solving for $\{s_r\}$ by substituting equations (A.1)–(A.3) in equation (19.b), we obtain,

$$([S_{38}] + [S_{NL18}])\{s_t\} + [S_{39}]\{s_r\} + [S_{40}]\{s_{r*}\} + [S_{41}]\{\phi\}$$
$$+ [S_{F8}](\{F_\psi\} - \{F_{T\psi}\}) = 0$$
$$([S_{42}] + [S_{NL20}])\{s_t\} + [S_{43}]\{s_r\} + [S_{44}]\{s_{r*}\} +$$
$$+ [S_{F11}](\{F_\psi\} - \{F_{T\psi}\}) - [S_{F10}](\{F_\phi\} - \{F_{T\phi}\}) = 0$$
$$([S_{45}] + [S_{NL22}])\{s_t\} + [S_{46}]\{s_r\} +$$
$$+ [S_{F15}](\{F_\psi\} - \{F_{T\psi}\}) - [S_{F14}](\{F_\phi\} - \{F_{T\phi}\}) = 0$$
$$\{s_r\} = \left(\begin{array}{l}-[S_{47}]\{s_t\} - [S_{NL\_23}]\{s_t\} - \\ [S_{F17}](\{F_\psi\} - \{F_{t\psi}\}) + [S_{F16}](\{F_\phi\} - \{F_{t\phi}\})\end{array}\right)$$
$$(A.4)$$

Finally, using equations (A.1)–(A.4) in equation (19.a), $\{s_t\}$ is derived along with the equivalent matrices $[S_{eq}]$ and $[S_{NL\_eq}]$ as follows:

$$([S_{48}] + [S_{NL\_24}])\{d_t\} + ([S_{49}] + [S_{NL\_25}])\{d_r\}$$
$$+ ([S_{50}] + [S_{NL\_26}])\{d_{r*}\} +$$
$$([S_{51}] + [S_{NL\_27}])\{\phi\} + [S_{F20}](\{F_\psi\} - \{F_{t\psi}\}) = \{F_t\}$$
$$([S_{52}] + [S_{NL\_29}])\{s_t\} + ([S_{53}] + [S_{NL\_30}])\{s_r\}$$
$$+ ([S_{54}] + [S_{NL\_31}])\{s_{r*}\} +$$
$$+ [S_{F26}](\{F_\psi\} - \{F_{t\psi}\}) - [S_{F25}](\{F_\phi\} - \{F_{T\phi}\}) = \{F_T\}$$
$$([S_{55}] + [S_{NL\_33}])\{s_t\} + ([S_{56}] + [S_{NL\_34}])\{s_r\} +$$
$$+ [S_{F32}](\{F_\psi\} - \{F_{T\psi}\}) - [S_{F31}](\{F_\phi\} - \{F_{T\phi}\}) = \{F_T\}$$
$$[S_{eq}]\{s_t\} + [S_{NL\_eq}]\{s_t\} = \{F_{eq}\}$$
$$\{s_t\} = ([S_{eq}] + [S_{NL\_eq}])^{-1}\{F_{eq}\}$$
$$(A-5)$$

## Appendix B

The different stiffness matrices leading to linear equivalent stiffness matrix $[S_{L\_eq}]$ can be denoted as,

$$[S_1^e] = [S_{tb1}^e] + [S_{ts1}^e]; [S_2^e] = [S_{rtb24}^e]^T + [S_{rts13}^e]^T$$

$$[S_3^e] = [S_{rtb4}^e]^T + [S_{rts3}^e]^T; [S_4^e] = [S_{tb\phi1}^e]^T + [S_{ts\phi1}^e]^T$$

$$[S_5^e] = [S_{tb\psi1}^e]^T + [S_{ts\psi1}^e]^T; [S_6^e] = [S_{rtb24}^e] + [S_{rts13}^e]$$

$$[S_7^e] = [S_{rrb3557}^e] + [S_{rrs3513}^e]; [S_8^e] = [S_{rrb57}^e] + [S_{rrs35}^e]$$

$$[S_9^e] = [S_{rb\phi24}^e]^T + [S_{r\phi s13}^e]^T; [S_{10}^e] = [S_{rb\psi24}^e]^T + [S_{r\psi s13}^e]^T$$

$$[S_{11}^e] = [S_{rtb4}^e] + [S_{rts3}^e]; [S_{12}^e] = [S_{rrb57}^e] + [S_{rrs35}^e]$$

$$[S^e_{13}] = [S^e_{rrb7}] + [S^e_{rrs5}]; \quad [S^e_{14}] = [S^e_{rb\phi4}]^T + [S^e_{r\phi s3}]^T$$

$$[S^e_{15}] = [S^e_{rb\psi4}]^T + [S^e_{r\psi s3}]^T; \quad [S^e_{16}] = [S^e_{tb\phi1}]^T + [S^e_{ts\phi1}]^T$$

$$[S^e_{17}] = [S^e_{rb\phi2}]^T + [S^e_{rb\phi4}]^T + [S^e_{r\phi s1}]^T + [S^e_{r\phi s3}]^T;$$
$$[S^e_{18}] = [S^e_{rb\phi4}]^T + [S^e_{r\phi s3}]^T; \quad [S^e_{19}] = [S^e_{tb\psi1}]^T + [S^e_{ts\psi1}]^T$$

$$[S^e_{20}] = [S^e_{rb\psi2}]^T + [S^e_{rb\psi4}]^T + [S^e_{r\psi s1}]^T + [S^e_{r\psi s3}]^T;$$

$$[S^e_{21}] = [S^e_{rb\psi4}]^T + [S^e_{r\psi s3}]^T;$$
$$[S^e_{22}] = \left([S_{16}] - [S_{\phi\psi}][S_{\psi\psi}]^{-1}[S_{19}]\right)$$

$$[S^e_{23}] = [S^e_{17}] - [S^e_{\phi\psi}][S^e_{\psi\psi}]^{-1}[S^e_{20}],$$

$$[S^e_{24}] = [S^e_{18}] - [S^e_{\phi\psi}][S^e_{\psi\psi}]^{-1}[S^e_{21}],$$

$$[S^e_{25}] = [S^e_{\phi\phi}] - [S^e_{\phi\psi}][S^e_{\psi\psi}]^{-1}[S^e_{\phi\psi}]^T$$

$$[S^e_{26}] = [S^e_{25}]^{-1}[S^e_{22}]^T; \quad [S^e_{27}] = [S^e_{25}]^{-1}[S^e_{23}]^T;$$
$$[S^e_{28}] = [S^e_{25}]^{-1}[S^e_{24}]^T$$

$$[S^e_{29}] = [S^e_{11}] - [S^e_{15}][S^e_{\psi\psi}]^{-1}[S^e_{19}];$$

$$[S^e_{30}] = [S^e_{12}] - [S^e_{15}][S^e_{\psi\psi}]^{-1}[S^e_{20}]$$

$$[S^e_{31}] = [S^e_{13}] - [S^e_{15}][S^e_{\psi\psi}]^{-1}[S^e_{21}];$$

$$[S^e_{32}] = [S^e_{14}] - [S^e_{15}][S^e_{\psi\psi}]^{-1}[S^e_{\phi\psi}]^T$$

$$[S^e_{33}] = [S^e_{29}] - [S^e_{32}][S^e_{26}]; \quad [S^e_{34}] = [S^e_{30}] - [S^e_{32}][S^e_{27}]$$

$$[S^e_{35}] = [S^e_{31}] - [S^e_{32}][S^e_{28}]; \quad [S^e_{36}] = [S^e_{35}]^{-1}[S^e_{33}]^T;$$

$$[S^e_{37}] = [S^e_{35}]^{-1}[S^e_{34}]^T; \quad [S^e_{38}] = [S^e_6] - [S^e_{10}][S^e_{\psi\psi}]^{-1}[S^e_{19}];$$

$$[S^e_{39}] = [S^e_7] - [S^e_{10}][S^e_{\psi\psi}]^{-1}[S^e_{20}];$$

$$[S^e_{40}] = [S^e_8] - [S^e_{10}][S^e_{\psi\psi}]^{-1}[S^e_{21}];$$

$$[S^e_{41}] = [S^e_9] - [S^e_{10}][S^e_{\psi\psi}]^{-1}[S^e_{\phi\psi}]^T;$$
$$[S^e_{42}] = [S^e_{38}] - [S^e_{41}][S^e_{26}]$$

$$[S^e_{43}] = [S^e_{39}] - [S^e_{41}][S^e_{27}]; \quad [S^e_{44}] = [S^e_{40}] - [S^e_{41}][S^e_{28}]$$

$$[S^e_{45}] = [S^e_{42}] - [S^e_{44}][S^e_{36}]; \quad [S^e_{46}] = [S^e_{43}] - [S^e_{44}][S^e_{37}]$$

$$[S^e_{47}] = [S^e_{46}]^{-1}[S^e_{45}]; \quad [S^e_{48}] = [S^e_1] - [S^e_5][S^e_{\psi\psi}]^{-1}[S^e_{19}]$$

$$[S^e_{49}] = [S^e_2] - [S^e_5][S^e_{\psi\psi}]^{-1}[S^e_{20}];$$
$$[S^e_{50}] = [S^e_3] - [S^e_5][S^e_{\psi\psi}]^{-1}[S^e_{21}][S^e_{51}]$$
$$= [S^e_4] - [S^e_5][S^e_{\psi\psi}]^{-1}[S^e_{\phi\psi}]^T;$$
$$[S^e_{52}] = [S^e_{48}] - [S^e_{51}][S^e_{26}]$$

$$[S^e_{53}] = [S^e_{49}] - [S^e_{51}][S^e_{27}]; \quad [S^e_{54}] = [S^e_{50}] - [S^e_{51}][S^e_{28}]$$

$$[S^e_{55}] = [S^e_{52}] - [S^e_{54}][S^e_{36}]; \quad [S^e_{56}] = [S^e_{53}] - [S^e_{54}][S^e_{37}]$$

$$[S^e_{L\_eq}] = [S^e_{55}] - [S^e_{56}][S^e_{47}] \tag{B.1}$$

Similarly, the matrices giving rise to the equivalent nonlinear stiffness matrix $[S_{NL\_eq}]$ can be written as follows:

$$[S^e_{NL\_1}] = [S^e_{tbNLbNL1\_tbtbNL1}]; \quad [S^e_{NL\_2}] = [S^e_{rbNL\_rtb24}]^T$$

$$[S^e_{NL\_3}] = [S^e_{rbNL4}]^T; \quad [S^e_{NL\_4}] = [S^e_{bNL\phi1}]$$

$$[S^e_{NL\_5}] = [S^e_{bNL\psi1}]; \quad [S^e_{NL\_6}] = [S^e_{rbNL24}]^T$$

$$[S^e_{NL\_7}] = [S^e_{rbNL4}]^T; \quad [S^e_{NL\_8}] = [S^e_{bNL\phi1}]^T;$$
$$[S^e_{NL\_9}] = [S^e_{bNL\psi1}]^T$$

$$[S^e_{NL\_10}] = [S^e_{\phi\psi}][S^e_{\psi\psi}]^{-1}[S^e_{NL\_9}],$$
$$[S^e_{NL\_11}] = [S^e_{NL\_8}] - [S^e_{NL\_10}]$$

$$[S^e_{NL\_12}] = [S^e_{25}]^{-1}[S^e_{NL\_11}];$$
$$[S^e_{NL\_13}] = [S^e_{NL\_7}] - [S^e_{15}][S^e_{\psi\psi}]^{-1}[S^e_{NL\_9}];$$

$$[S^e_{NL\_14}] = [S^e_{32}][S^e_{NL\_12}];$$
$$[S^e_{NL\_15}] = [S^e_{NL\_14}] - [S^e_{NL\_13}];$$

$$[S^e_{NL\_16}] = [S^e_{35}]^{-1}[S^e_{NL\_15}];$$
$$[S^e_{NL\_17}] = [S^e_{10}][S^e_{\psi\psi}]^{-1}[S^e_{NL\_9}];$$

$$[S^e_{NL\_18}] = [S^e_{NL\_6}] - [S^e_{NL\_17}];$$
$$[S^e_{NL\_19}] = [S^e_{41}][S^e_{NL\_12}];$$

$[S^e_{NL\_20}] = [S^e_{NL\_19}] - [S^e_{NL\_18}];$
$[S^e_{NL\_21}] = [S^e_{44}][S^e_{NL\_16}];$

$[S^e_{NL\_22}] = [S^e_{NL\_20}] - [S^e_{NL\_21}];$
$[S^e_{NL\_23}] = [S^e_{46}]^{-1}[S^e_{NL\_22}];$

$[S^e_{NL\_24}] =$
$$\left( \begin{array}{l} [S^e_{NL\_1}] - [S^e_{NL\_5}]\left[S^e_{\psi\psi}\right]^{-1}[S^e_{19}] - [S^e_5]\left[S^e_{\psi\psi}\right]^{-1}[S^e_{NL\_9}] - \\ [S^e_{NL\_5}]\left[S^e_{\psi\psi}\right]^{-1}[S^e_{NL\_9}] \end{array} \right)$$

$[S^e_{NL\_25}] = [S^e_{NL\_2}] - [S^e_{NL\_5}]\left[S^e_{\psi\psi}\right]^{-1}[S^e_{20}]$

$[S^e_{NL\_26}] = [S^e_{NL\_3}] - [S^e_{NL\_5}]\left[S^e_{\psi\psi}\right]^{-1}[S^e_{21}]$
$[S^e_{NL\_27}] = [S^e_{NL\_4}] - [S^e_{NL\_5}]\left[S^e_{\psi\psi}\right]^{-1}[S^e_{\psi\phi}]$

$[S^e_{NL\_28}] = [S^e_{51}][S^e_{NL\_12}]$

$[S^e_{NL\_29}] = -[S^e_{NL\_28}] + [S^e_{NL\_24}] - [S^e_{NL\_27}][S^e_{26}]$
$\qquad\qquad - [S^e_{NL\_27}][S^e_{NL\_12}]$
$[S^e_{NL\_30}] = [S^e_{NL\_25}] - [S^e_{NL\_27}][S^e_{27}],$
$[S^e_{NL\_31}] = [S^e_{NL\_26}] - [S^e_{NL\_27}][S^e_{28}];$

$[S^e_{NL\_32}] = [S^e_{54}][S^e_{NL\_16}];$

$[S^e_{NL\_33}] = [S^e_{NL\_29}] - [S^e_{NL\_32}] - [S^e_{NL\_31}][S^e_{36}]$
$\qquad\qquad - [S^e_{NL\_31}][S^e_{NL\_16}]$

$[S^e_{NL\_34}] = [S^e_{NL\_30}] - [S^e_{NL\_31}][S^e_{37}]$

$[S^e_{NL\_35}] = [S^e_{56}][S^e_{NL\_23}], [S^e_{NL\_36}] = [S^e_{NL\_34}][S^e_{47}]$

$[S^e_{NL\_37}] = [S^e_{NL\_34}][S^e_{NL\_23}]$

$\left[S^e_{NL\_eq}\right] = [S^e_{NL\_33}] - [S^e_{NL\_35}] - [S^e_{NL\_36}] - [S^e_{NL\_37}]$
$$\tag{B.2}$$

The matrices contributing to the equivalent force $\{F_{eq}\}$ are,

$$\{F_{eq}\} = \{F_T\} - \left[S^e_{F\phi}\right]\left(\{F_\phi\} + \{F_{T\phi}\}\right)$$
$$- \left[S^e_{F\psi}\right]\left(\{F_\psi\} + \{F_{T\psi}\}\right)$$

where,

$\left[S^e_{F\phi}\right] = [S^e_{F31}] - [S^e_{F35}] - [S^e_{F33}];$
$\left[S^e_{F\psi}\right] = [S^e_{F32}] - [S^e_{F36}] - [S^e_{F34}]$

$[S^e_{F1}] = [S^e_{25}]^{-1}[S^e_{\phi\psi}]\left[S^e_{\psi\psi}\right]^{-1}; [S^e_{F2}] = [S^e_{15}]\left[S^e_{\psi\psi}\right]^{-1}$

$[S^e_{F3}] = [S^e_{32}][S^e_{25}]^{-1}; [S^e_{F4}] = [S^e_{32}][S^e_{F1}]$

$[S^e_{F5}] = [S^e_{F2}] - [S^e_{F4}]; [S^e_{F6}] = [S^e_{35}]^{-1}[S^e_{F5}]$

$[S^e_{F7}] = [S^e_{35}]^{-1}[S^e_{F3}]; [S^e_{F8}] = [S^e_{10}]\left[S^e_{\psi\psi}\right]^{-1}$

$[S^e_{F9}] = [S^e_{41}][S^e_{F1}]; [S^e_{F10}] = [S^e_{41}][S^e_{25}]^{-1};$
$[S^e_{F11}] = [S^e_{F8}] - [S^e_{F9}]; [S^e_{F12}] = [S^e_{44}][S^e_{F6}];$

$[S^e_{F13}] = [S^e_{44}][S^e_{F7}]; [S^e_{F14}] = [S^e_{F10}] - [S^e_{F13}]$

$[S^e_{F15}] = [S^e_{F11}] - [S^e_{F12}]; [S^e_{F16}] = [S^e_{46}]^{-1}[S^e_{F14}];$

$[S^e_{F17}] = [S^e_{46}]^{-1}[S^e_{F15}]; [S^e_{F18}] = [S^e_5]\left[S^e_{\psi\psi}\right]^{-1}$

$[S^e_{F19}] = [S^e_{NL\_5}]\left[S^e_{\psi\psi}\right]^{-1}; [S^e_{F20}] = [S^e_{F18}] + [S^e_{F19}]$

$[S^e_{F21}] = [S^e_{51}][S^e_{F1}]; [S^e_{F22}] = [S^e_{51}][S^e_{25}]^{-1}$

$[S^e_{F23}] = [S^e_{NL\_27}][S^e_{F1}]; [S^e_{F24}] = [S^e_{NL\_27}][S^e_{25}]^{-1}$

$[S^e_{F25}] = [S^e_{F22}] + [S^e_{F24}]; [S^e_{F26}] = [S^e_{F20}] - [S^e_{F21}] - [S^e_{F23}]$

$[S^e_{F27}] = [S^e_{54}][S^e_{F6}]; [S^e_{F28}] = [S^e_{54}][S^e_{F7}]$

$[S^e_{F29}] = [S^e_{NL\_31}][S^e_{F6}]; [S^e_{F30}] = [S^e_{NL\_31}][S^e_{F7}]$

$[S^e_{F31}] = [S^e_{F25}] + [S^e_{F30}] + [S^e_{F28}];$
$[S^e_{F32}] = [S^e_{F26}] - [S^e_{F29}] - [S^e_{F27}];$
$[S^e_{F33}] = [S^e_{56}][S^e_{F16}]; [S^e_{F34}] = [S^e_{56}][S^e_{F17}];$
$[S^e_{F35}] = [S^e_{NL\_34}][S^e_{F16}];$

$[S^e_{F36}] = [S^e_{NL\_34}][S^e_{F17}],$

$[S^e_{F37}] = [S^e_{F32}] - [S^e_{F34}] - [S^e_{F36}]$
$$\tag{B.3}$$

$[S^e_{F38}] = [S^e_{F33}] + [S^e_{F35}] - [S^e_{F31}]$

$$[S^e_{rrs35}] = [S^e_{rrs3}] + [S^e_{rrs5}], [S^e_{rrs13}] = [S^e_{rrs1}] + [S^e_{rrs3}],$$
$$[S^e_{rrs3513}] = [S^e_{rrs35}] + [S^e_{rrs13}], [S^e_{rts13}] = [S^e_{rts1}] + [S^e_{rts3}]$$

$$\left[S^e_{r\psi s13}\right] = \left[S^e_{r\psi s1}\right] + \left[S^e_{r\psi s3}\right], \left[S^e_{r\phi s13}\right] = \left[S^e_{r\phi s1}\right] + \left[S^e_{r\phi s3}\right]$$

$$[S^e_{tbtbNL1}] = [S^e_{tb1}] + [S^e_{tbNL1}],$$
$$[S^e_{rtb24}] = [S^e_{rtb2}] + [S^e_{rtb4}]$$

$$[S^e_{tbNLbNL1\_tbtbNL1}] = [S^e_{tbNLbNL1}] + [S^e_{tbtbNL1}],$$
$$[S^e_{rbNL\_rtb24}] = [S^e_{rbNL24}] + [S^e_{rtb24}],$$
$$[S^e_{rbNL\_rtb4}] = [S^e_{rbNL4}] + [S^e_{rtb4}]$$

$$\left[S^e_{bNL\_tb\phi1}\right] = \left[S^e_{bNL\phi1}\right] + \left[S^e_{tb\phi1}\right],$$
$$\left[S^e_{bNL\_tb\psi1}\right] = \left[S^e_{bNL\psi1}\right] + \left[S^e_{tb\psi1}\right]$$

$$[S^e_{rrb57}] = [S^e_{rrb5}] + [S^e_{rrb7}],$$
$$[S^e_{rtbrbNL4}] = [S^e_{rtb4}] + [S^e_{rbNL4}]$$

$$[S^e_{rtbrbNL2}] = [S^e_{rtb2}] + [S^e_{rbNL2}],$$
$$[S^e_{rtbrbNL24}] = [S^e_{rtbrbNL2}] + [S^e_{rtbrbNL4}]$$

$$[S^e_{rrb35}] = [S^e_{rrb3}] + [S^e_{rrb5}],$$
$$[S^e_{rrb5735}] = [S^e_{rrb57}] + [S^e_{rrb35}]$$

$$\left[S^e_{rb\phi24}\right] = \left[S^e_{rb\phi2}\right] + \left[S^e_{rb\phi4}\right],$$
$$\left[S^e_{rb\psi24}\right] = \left[S^e_{rb\psi2}\right] + \left[S^e_{rb\psi4}\right]$$

$$[S^e_{tbNLbNL1}] = [S^e_{tbNL1}] + [S^e_{bNL1}],$$
$$[S^e_{rbNL24}] = [S^e_{rbNL2}] + [S^e_{rbNL4}]$$

$$(B.4)$$

where,

$$[S^e_{rtb4}] = \int_0^a \int_0^b [SD_{rb}]^T [D_{b4}][SD_{tb}] dxdy;$$

$$[S^e_{rbNL4}] = \int_0^a \int_0^b [SD_{rb}]^T [D_{bNL4}][SD_1][SD_2] dxdy$$

$$[S^e_{rrb5}] = \int_0^a \int_0^b [SD_{rb}]^T [D_{b5}][SD_{rb}] dxdy;$$

$$[S^e_{rrb7}] = \int_0^a \int_0^b [SD_{rb}]^T [D_{b7}][SD_{rb}] dxdy$$

$$\left[S^e_{rb\phi4}\right] = \int_0^a \int_0^b [SD_{rb}]^T [D_{b\phi4}] [SD_\phi] dxdy;$$

$$\left[S^e_{rb\psi4}\right] = \int_0^a \int_0^b [SD_{rb}]^T [D_{b\psi4}] [SD_\psi] dxdy$$

$$[S^e_{rtb4}] = \int_0^a \int_0^b [SD_{rb}]^T [D_{b4}][SD_{tb}] dxdy;$$

$$[S^e_{rtb2}] = \int_0^a \int_0^b [SD_{rb}]^T [D_{b2}][SD_{tb}] dxdy$$

$$[S^e_{rbNL2}] = \int_0^a \int_0^b [SD_{rb}]^T [D_{bNL2}][SD_1][SD_2] dxdy;$$

$$[S^e_{rrb3}] = \int_0^a \int_0^b [SD_{rb}]^T [D_{b3}][SD_{rb}] dxdy$$

$$[S^e_{rrb5}] = \int_0^a \int_0^b [SD_{rb}]^T [D_{b5}][SD_{rb}] dxdy;$$

$$\left[S^e_{rb\phi2}\right] = \int_0^a \int_0^b [SD_{rb}]^T [D_{b\phi2}] [SD_\phi] dxdy$$

$$\left[S^e_{rb\psi2}\right] = \int_0^a \int_0^b [SD_{rb}]^T [D_{b\psi2}] [SD_\psi] dxdy;$$

$$[S^e_{tbNL1}] = \int_0^a \int_0^b [SD_{tb}]^T [D_{bNL1}][SD_1][SD_2] dxdy$$

$$[S^e_{bNL1}] = \int_0^a \int_0^b [SD_2]^T [SD_1]^T [D_{bbNL1}][SD_1][SD_2] dxdy;$$

$$\left[S^e_{bNL\phi1}\right] = \int_0^a \int_0^b [SD_\phi]^T [D_{bNL\phi1}][SD_1][SD_2] dxdy;$$

$$\left[S^e_{bNL\psi1}\right] = \int_0^a \int_0^b [SD_\psi]^T [D_{bNL\psi1}][SD_1][SD_2] dxdy$$

$$[S^e_{tb1}] = \int_0^a \int_0^b [SD_{tb}]^T [D_{b1}][SD_{tb}] dxdy;$$

$$\left[S^e_{tb\phi1}\right] = \int_0^a \int_0^b [SD_{tb}]^T [D_{b\phi1}] [SD_\phi] dxdy$$

$$\left[S^e_{tb\psi 1}\right] = \int_0^a \int_0^b [SD_{tb}]^T [D_{b\psi 1}][SD_\psi] \, dxdy;$$

$$\left[S^e_{rts3}\right] = \int_0^a \int_0^b [SD_{rs}]^T [D_{s3}][SD_{ts}] \, dxdy$$

$$[S_{rrs3}] = \int_0^a \int_0^b [SD_{rs}]^T [D_{s3}][SD_{rs}] \, dxdy;$$

$$\left[S^e_{rrs5}\right] = \int_0^a \int_0^b [SD_{rs}]^T [D_{s5}][SD_{rs}] \, dxdy$$

$$[S_{r\psi s3}] = \int_0^a \int_0^b [SD_{rs}]^T [D_{s\psi 3}][SD_\psi] \, dxdy;$$

$$\left[S^e_{r\phi s3}\right] = \int_0^a \int_0^b [SD_{rs}]^T [D_{s\phi 3}][SD_\phi] \, dxdy$$

$$\left[S^e_{ts\phi 1}\right] = \int_0^a \int_0^b [SD_{ts}]^T [D_{s\phi 1}][SD_\phi] \, dxdy;$$

$$\left[S^e_{ts\psi 1}\right] = \int_0^a \int_0^b [SD_{ts}]^T [D_{s\psi 1}][SD_\psi] \, dxdy$$

$$\left[S^e_{r\phi s1}\right] = \int_0^a \int_0^b [SD_{rs}]^T [D_{s\phi 1}][SD_\phi] \, dxdy;$$

$$[S_{r\psi s1}] = \int_0^a \int_0^b [SD_{rs}]^T [D_{s\psi 1}][SD_\psi] \, dxdy$$

$$\left[S^e_{rts1}\right] = \int_0^a \int_0^b [SD_{rs}]^T [D_{s1}][SD_{ts}] \, dxdy;$$

$$\left[S^e_{rrs1}\right] = \int_0^a \int_0^b [SD_{rs}]^T [D_{s1}][SD_{rs}] \, dxdy$$

$$[S_{ts1}] = \int_0^a \int_0^b [SD_{ts}]^T [D_{s1}][SD_{ts}] \, dxdy;$$

$$\left[S^e_{rts3}\right] = \int_0^a \int_0^b [SD_{rs}]^T [D_{s3}][SD_{ts}] \, dxdy$$

$$\{F_\psi\} = \int_0^a \int_0^b [N_\psi]^T Q^\psi \, dxdy; \{F_\phi\} = \int_0^a \int_0^b [N_\phi]^T Q^\phi \, dxdy;$$

$$\{F_t\} = \int_{\Omega^N} [C_b]^N [\alpha]^N \Delta T d\Omega^N; \{F_{t\phi}\} = \int_{\Omega^N} [p] \Delta T d\Omega^N;$$

$$\{F_{t\psi}\} = \int_{\Omega^N} [\tau] \Delta T d\Omega^N;$$

(B.5)

The rigidity matrices appearing in equation (B.5) can be written as follows:

$$[D_{b1}] = \sum_{N=1}^3 \int_{-h/2}^{h/2} [C_b]^N dz; [D_{bbNL1}] = \frac{1}{4}[D_{b1}];$$

$$[D_{bNL1}] = \frac{1}{2}[D_{b1}]; [D_{b2}] = \sum_{N=1}^3 \int_{-h/2}^{h/2} z[C_b]^N dz;$$

$$[D_{bNL2}] = \frac{1}{2}[D_{b2}]; [D_{b3}] = \sum_{N=1}^3 \int_{-h/2}^{h/2} z^2 [C_b]^N dz;$$

$$[D_{b4}] = \sum_{N=1}^3 \int_{-h/2}^{h/2} c_1 z^3 [C_b]^N dz; [D_{bNL4}] = \frac{1}{2}[D_{b4}];$$

$$[D_{b5}] = \sum_{N=1}^3 \int_{-h/2}^{h/2} c_1 z^4 [C_b]^N dz;$$

$$[D_{b7}] = \sum_{N=1}^3 \int_{-h/2}^{h/2} c_1^2 z^6 [C_b]^N dz;$$

$$[D_{b\phi 1}] = \int_{h_3}^{h_4} [Z_t][e_b]dz + \int_{h_1}^{h_2} [Z_b][e_b]dz;$$

$$[D_{bNL\phi 1}] = [D_{b\phi 1}];$$

$$[D_{b\phi 2}] = \int_{h_3}^{h_4} z[Z_t][e_b]dz + \int_{h_1}^{h_2} z[Z_b][e_b]dz;$$

$$[D_{b\phi 4}] = \int_{h_3}^{h_4} c_1 z^3 [Z_t][e_b]dz + \int_{h_1}^{h_2} c_1 z^3 [Z_b][e_b]dz;$$

$$[D_{s1}] = \sum_{N=1}^3 \int_{-h/2}^{h/2} [C_s]^N dz;$$

$$[D_{b\psi 1}] = \int_{h_3}^{h_4} [Z_t][q_b]dz + \int_{h_1}^{h_2} [Z_b][q_b]dz;$$

$$[D_{bNL\psi 1}] = [D_{b\psi 1}];$$

$$[D_{b\psi 2}] = \int_{h_3}^{h_4} z[Z_t][q_b]dz + \int_{h_1}^{h_2} z[Z_b][q_b]dz;$$

$$[D_{b\psi 4}] = \int_{h_3}^{h_4} c_1 z^3[Z_t][q_b]dz + \int_{h_1}^{h_2} c_1 z^3[Z_b][q_b]dz;$$

$$[D_{s3}] = \sum_{N=1}^{3} \int_{-h/2}^{h/2} c_2 z^2 [C_s]^N dz;$$

$$[D_{s5}] = \sum_{N=1}^{3} \int_{-h/2}^{h/2} c_2{}^2 z^4 [C_s]^N dz;$$

$$[D_{s\phi 1}] = \int_{h_3}^{h_4} [Z_t][e_s]^T dz + \int_{h_1}^{h_2} [Z_b][e_s]^T dz;$$

$$[D_{s\phi 3}] = \int_{h_3}^{h_4} c_2 z^2[Z_t][e_s]^T dz + \int_{h_1}^{h_2} c_2 z^2[Z_b][e_s]^T dz;$$

$$[D_{s\psi 1}] = \int_{h_3}^{h_4} [Z_t][q_s]^T dz + \int_{h_1}^{h_2} [Z_b][q_s]^T dz;$$

$$[D_{s\psi 3}] = \int_{h_3}^{h_4} c_2 z^2[Z_t][q_s]^T dz + \int_{h_1}^{h_2} c_2 z^2[Z_b][q_s]^T dz;$$

$$[D_{\phi\phi}] = \int_{h_3}^{h_4} [Z_t]^T[\eta][Z_t]dz + \int_{h_1}^{h_2} [Z_b]^T[\eta][Z_b]dz;$$

$$[D_{\psi\psi}] = \int_{h_3}^{h_4} [Z_t]^T[\mu][Z_t]dz + \int_{h_1}^{h_2} [Z_b]^T[\mu][Z_b]dz;$$

$$[D_{\phi\psi}] = \int_{h_3}^{h_4} [Z_t]^T[m][Z_t]dz + \int_{h_1}^{h_2} [Z_b]^T[m][Z_b]dz;$$

$$(B.6)$$

The derivative of shape function matrices appearing in the FE formulation can be represented by

$$[SD_{tb}] = \begin{bmatrix} N_{i,x} & 0 & 0 \\ 0 & N_{i,y} & 0 \\ N_{i,y} & N_{i,x} & 0 \end{bmatrix}, [SD_{rb}] = \begin{bmatrix} N_{i,x} & 0 \\ 0 & N_{i,y} \\ N_{i,y} & N_{i,x} \end{bmatrix},$$

$$[SD_{ts}] = \begin{bmatrix} 0 & 0 & N_{i,x} \\ 0 & 0 & N_{i,y} \end{bmatrix}, [SD_{rs}] = \begin{bmatrix} 1 & 0 \\ 0 & 1 \end{bmatrix}$$

$$[SD_1] = \begin{bmatrix} w_{0,x} & 0 & w_{0,y} \\ 0 & w_{0,y} & w_{0,x} \end{bmatrix}^T,$$

$$[B_2] = [SD_{21} \quad SD_{22} \quad \cdots \quad SD_{28}]; [SD_\phi] = [SD_\psi]$$

$$= \begin{bmatrix} N_{i,x} \\ N_{i,y} \\ N_{i,z} \end{bmatrix}$$

$$(B.7)$$